

Rapid onset of a Comptonisation zone in the repeating tidal disruption event XMMSL2 J140446.9-251135

R. D. Saxton^{1*}, T. Wevers^{2,3}, S. van Velzen⁴, K. Alexander⁵, Z. Liu^{6,7}, A. Mummery⁸, M. Giustini⁹, G. Miniutti⁹, F. Fuerst¹⁰, J. J. E. Kajava¹¹, A. M. Read¹², P. G. Jonker¹³, A. Rau⁶, and D.-Y. Li¹⁴

¹ Telespazio UK for ESA, ESAC, Apartado 78, 28691 Villanueva de la Cañada, Madrid, Spain

² Astrophysics & Space Institute, Schmidt Sciences, New York, NY 10011, USA.

³ Space Telescope Science Institute, 3700 San Martin Drive, Baltimore, MD 21218, USA.

⁴ Leiden Observatory, Leiden University, PO Box 9513, 2300 RA Leiden, The Netherlands

⁵ Department of Astronomy and Steward Observatory, University of Arizona, 933 North Cherry Avenue, Tucson, AZ 85721-0065, USA

⁶ Max-Planck-Institut für extraterrestrische Physik, Gießenbachstraße 1, 85748 Garching, Germany

⁷ Centre for Astrophysics Research, Department of Physics, Astronomy and Mathematics, University of Hertfordshire, College Lane, Hatfield, AL10 9AB, UK.

⁸ University of Oxford, Dept. of Physics, Denys Wilkinson building, Keble road, OX1 3RU, Oxford, U.K.

⁹ Centro de Astrobiología (CAB), CSIC-INTA, Camino Bajo del Castillo s/n, ESAC campus, 28692 Villanueva de la Cañada, Madrid, Spain

¹⁰ ESA, ESAC, Apartado 78, 28691 Villanueva de la Cañada, Madrid, Spain

¹¹ SERCO for ESA, ESAC, Apartado 78, 28691 Villanueva de la Cañada, Madrid, Spain

¹² Dept. of Physics and Astronomy, University of Leicester, Leicester LE1 7RH, U.K.

¹³ Department of Astrophysics/IMAPP, Radboud University, P.O. Box 9010, 6500 GL, Nijmegen, The Netherlands

¹⁴ National Astronomical Observatories, Chinese Academy of Sciences, 20A Datun Road, Chaoyang District, Beijing, 100101, China

Received date /Accepted date

ABSTRACT

We report here on observations of a tidal disruption event, XMMSL2 J1404-2511, discovered in an XMM-Newton slew, in a quiescent galaxy at $z = 0.043$. X-ray monitoring covered the epoch when the accretion disc transitioned from a thermal state, with $kT \sim 80$ eV, to a harder state dominated by a warm, optically-thick corona. The bulk of the coronal formation took place within 7 days and was coincident with a temporary drop in the emitted radiation by a factor 4. After a plateau phase of ~ 100 days, the X-ray flux of XMMSL2 J1404-2511 decayed by a factor 500 within 230 days. We estimate the black hole mass in the galaxy to be $M_{\text{BH}} = (4 \pm 2) \times 10^6 M_{\odot}$ and the peak X-ray luminosity $L_X \sim 6 \times 10^{43}$ ergs s⁻¹. The optical/UV light curve is flat over the timescale of the observations with $L_{\text{opt}} \sim 2 \times 10^{41}$ ergs s⁻¹. We find that TDEs with coronae are more often found in an X-ray sample than in an optically-selected sample. Late-time monitoring of the optical sample is needed to test whether this is an intrinsic property of TDEs or is due to a selection effect. From the fast decay of the X-ray emission we consider that the event was likely due to the partial stripping of an evolved star rather than a full stellar disruption, an idea supported by the detection of two further re-brightening episodes, two and four years after the first event, in the SRG/eROSITA all-sky survey.

Key words. X-rays: galaxies – Galaxies:individual:XMMSL2 J140446.9-251135 – Galaxies: nuclei – accretion discs

1. Introduction

A tidal disruption event (TDE) occurs when a star passes too close to a supermassive black hole and is disrupted by gravitational tidal forces (Hills 1975; Rees 1988; Ulmer 1999). Electromagnetic signals from TDEs have been detected at a wide range of wavelengths including radio (Alexander et al. 2020), infrared (Jiang et al. 2016; Li et al. 2020), optical (Arcavi et al. 2014; Holoien et al. 2014; Hammerstein et al. 2023), UV (Gezari et al. 2003) and X-rays (Komossa & Bade 1999; Esquej et al. 2008). X-ray emission is thought to primarily come from an accretion disc about the SMBH (Rees 1990; Cannizzo et al. 1990; Komossa 2015; Mummery & Balbus 2020; Wen et al. 2020; Saxton et al. 2021) although shocks between streams (Piran et al. 2015) or between tidal streams and a forming accretion disc (Steinberg & Stone 2022) may contribute at early

times, while interaction between outflowing material and a pre-existing dense medium has been suggested to contribute on multi-year timescales (Mou et al. 2021).

When first observed the X-ray spectrum can often be described purely by thermal disc emission with little or no hard X-ray emission from a corona (Komossa & Bade 1999; Holoien et al. 2016; Gezari et al. 2017; Guolo et al. 2024, see Mummery et al. 2023 for a sample). This is in contrast to active galactic nuclei (AGN) where coronal emission is nearly ubiquitous (Svoboda et al. 2017; Laha et al. 2024), indicating a fundamental difference in the properties of newly formed TDE accretion discs from mature persistently-fed discs. Many TDEs, particularly those discovered in optical surveys, remain in the thermal state throughout the whole of their monitoring (Guolo et al. 2024), sometimes in excess of a 1000 days (Bright et al. 2018; Wen et al. 2023; Wevers et al. 2024; Guolo & Mummery 2025). In some cases, higher cadence monitoring has revealed the for-

* E-mail: richard.saxton@ext.esa.int

mation of a harder component. AT2018fyk evolved from a thermal to power-law dominated spectrum in less than a hundred days (Wevers et al. 2021) while AT2021ehb gradually formed a dominant hard spectral component over 170 days which softened significantly within 3 days while the X-ray flux faded by an order of magnitude (Yao et al. 2022). Radio observations of these sources showed that the hard X-ray component is not related to a relativistic jet as was found to be the case for SWIFT J164449.3+573451 (Burrows et al. 2011; Bloom et al. 2011; Zauderer et al. 2013) (but see Christy et al. 2024). The interpretation is that hard X-rays are generated by the up-scattering of disc photons by a corona (e.g. Wevers et al. 2019). It is unclear why this component only appears to develop in a minority of TDEs, although the time needed to magnetically build the corona may be a factor (Yao et al. 2022).

These events give a view of the dynamic evolution of accretion structure around SMBH, which is otherwise only accessible in the rare changing-look AGN (CLAGN; Ricci & Trakhtenbrot 2022). State changes are particularly prevalent in partial TDEs (pTDE; Guillochon & Ramirez-Ruiz 2013), some of which show multiple peaks in their light curves indicating periodic stripping of material from an evolved star (Wevers et al. 2023; Liu et al. 2024). This can be understood in terms of each stripping providing a relatively low mass of material to the system, resulting in a rapid change of the accretion rate as material is consumed. Changes in accretion rate are believed to influence state changes seen in stellar mass black hole discs (Esin et al. 1997).

In this paper we describe a TDE discovered in the XMM-Newton slew survey, XMMSL2 J1404-2511, whose X-ray spectrum demonstrates a rapid build up of the corona shortly after detection.

In Section 2 we discuss the discovery of this TDE and the source identification; in Sections 3, 4 & 5 we present UV, optical, radio and X-ray follow-up observations and in Section 6 we discuss the source characteristics within the TDE model. The paper is summarised in Section 7.

A Λ CDM cosmology with $(\Omega_M, \Omega_\Lambda) = (0.27, 0.73)$ and $H_0 = 70 \text{ km}^{-1} \text{ s}^{-1} \text{ Mpc}^{-1}$ has been assumed throughout.

2. Discovery of XMMSL2 J1404-2511

A new source of X-rays, XMMSL2 J140446.9-251135 (hereafter XMMSL2 J1404-2511), was discovered by XMM-Newton (Jansen et al. 2001) while it slewed between targets on Feb 15 2018, with a count rate of $4.4 \pm 1.1 \text{ c/s}$ in the EPIC-pn camera (Read et al. 2018). The X-rays were located to a position RA: 14 04 46.68 DEC: -25 11 43.3 ($\pm 1.9 \text{ arcsec}$; 90% confidence) by follow-up observations with the Neil Gehrels Swift observatory (henceforth *Swift*; Gehrels et al. 2004) and shown to be coincident with the galaxy 2MASX 14044671-2511433 (Fig. 1).

The EPIC-pn slew spectrum was soft and could be fit with a black-body of $92_{-22}^{+30} \text{ eV}$ and 0.2–2 keV flux $5.6 \times 10^{-12} \text{ ergs s}^{-1} \text{ cm}^{-2}$ absorbed by the Galactic column of $N_H = 6.7 \times 10^{20} \text{ cm}^{-2}$ (Willingale et al. 2013). The ROSAT All Sky Survey (RASS) 2-sigma upper limit from 1990 was 0.033 c/s equating to a flux of $< 5 \times 10^{-13} \text{ ergs s}^{-1} \text{ cm}^{-2}$ using the same spectral model, a factor > 10 lower than the slew detection.

3. Optical and UV follow-up

An optical spectrum was taken by the NTT within the ePESSTO program (Smartt et al. 2015) on 2018-03-08 revealing a quies-

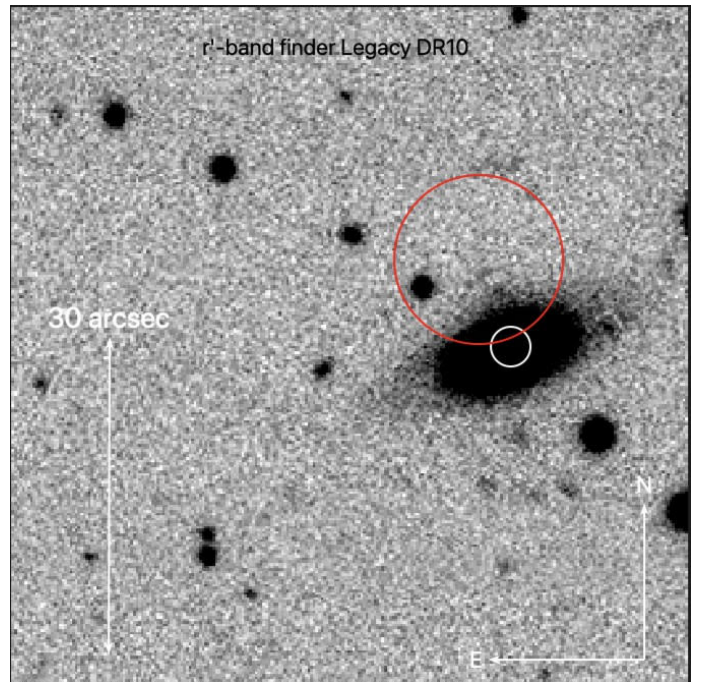


Fig. 1. Finder chart of XMMSL2 J1404-2511 based on an r' band image from the Legacy DR10 survey performed on DECam on the Blanco CT10 telescope. Red circle is the XMM-Newton slew error circle of 8 arcseconds radius and the white circle is the Swift-UVOT enhanced position with an error of 1.9 arcseconds.

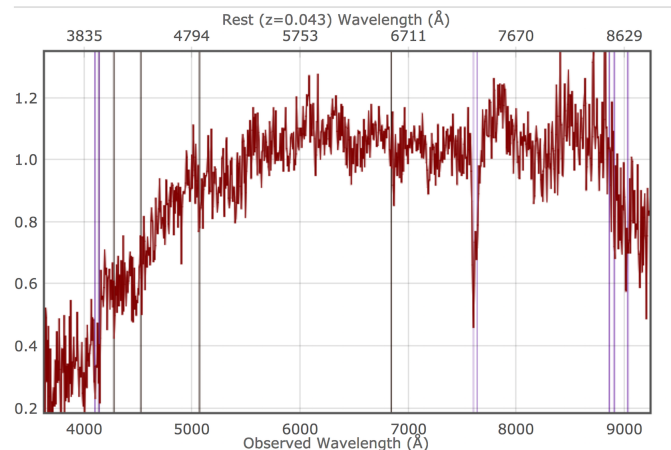


Fig. 2. Optical spectrum of 2MASX 1404-25 taken with the New Technology Telescope (NTT) on 2018-03-08 as part of the ePESSTO program.

cent galaxy with no emission lines at redshift $z = 0.043 \pm 0.001$ (Taubenberger et al. 2018; Fig. 2).

A further optical spectrum was taken with the MagE instrument on the Magellan telescope with a 0.7 arcsecond slit on 2020-02-15 (Wevers 2020; Fig. 3). Blaze corrections were performed for each individual échelle order by fitting a low order spline function to regions devoid of absorption and emission lines, after which the spectrum was stitched together using an inverse variance weighting scheme for overlapping wavelength ranges between orders. Following the procedures outlined in Wevers et al. (2017), the Penalized Pixel fitting routine (Cappellari 2017) was used in combination with the Elodie stellar template library (Prugniel et al. 2007) to measure the velocity dispersion of this continuum normalized spectrum, correct-

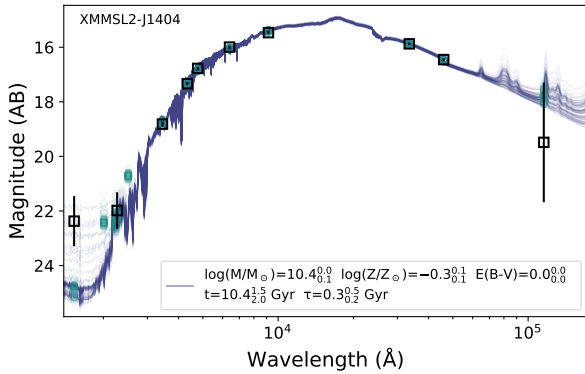


Fig. 3. Host galaxy photometry based on GALEX (Martin et al. 2005), DECaLS (Dey et al. 2019), and WISE (Wright et al. 2010; Mainzer et al. 2011). We also include the post-peak aperture photometry in the UVOT B- and U-band. We show samples from the posterior distribution of population synthesis galaxy models (Conroy et al. 2009; Johnson & Leja 2017), following the method outlined in van Velzen et al. (2021). The predicted magnitudes (including UVOT W1, M2, and W2) are shown with open circles.

ing for the instrumental broadening of $\sigma_{\text{inst}} = 22 \text{ km s}^{-1}$. A velocity dispersion of $93 \pm 1 \text{ km/s}$ was measured. Using the $M - \sigma$ relation of Gültekin et al. (2009) a black hole mass of $\log_{10}(M_{\text{BH}}) = 6.71 \pm 0.4 M_{\odot}$ is obtained with the error dominated by the systematic error of the method¹.

Photometric observations were made with the Swift ultraviolet telescope (UVOT; Tab. 1) and with the XMM-Newton optical monitor (XMM-OM). In both telescopes the B, U, UVW1, UVM2 and UVW2 filters were used and UVOT also observed with the V filter (Fig. 4). The galaxy was faint being detected in all of the UVOT filters but not in the XMM-OM camera in the UVW2 or UVM2 filters. The UV temperature, obtained by fitting all UVOT data simultaneously to a power-law decay and a single black-body is $T = 10^{4.4 \pm 0.1} \text{ K}$, which is at the high end of the distribution of temperatures seen in a sample of 30 spectroscopically-classified ZTF TDEs (Hammerstein et al. 2023). The black-body integrated optical/UV luminosity of $L_{\text{bb}} \sim 2 \times 10^{41} \text{ ergs s}^{-1}$ evolves slowly and if the optical emission did have a peak then that peak would have occurred well before the first X-ray observation (Fig. 4).

The GALEX catalogue (Bianchi et al. 2017) contains a source (GALEX J140446.5-251140) at an offset of 4 arcseconds from 2MASX 1404-25, detected in the NUV filter with magnitude 21.81 ± 0.65 on 2007-05-12 but undetected in the FUV filter.

Historical optical observations from the All-Sky Automated Survey for SuperNovae (ASAS-SN; Shappee et al. 2014) are flat from 2014 until 2022, although we note that the light curve has a gap between 2017-08-19 and 2017-12-17 (Fig. 4). No Gaia science alert² was triggered for XMMSL2 J1404-2511 also indicating that the source has not brightened by more than 1 magnitude in the Gaia G band since the alerts started in 2016 (Hodgkin et al. 2021).

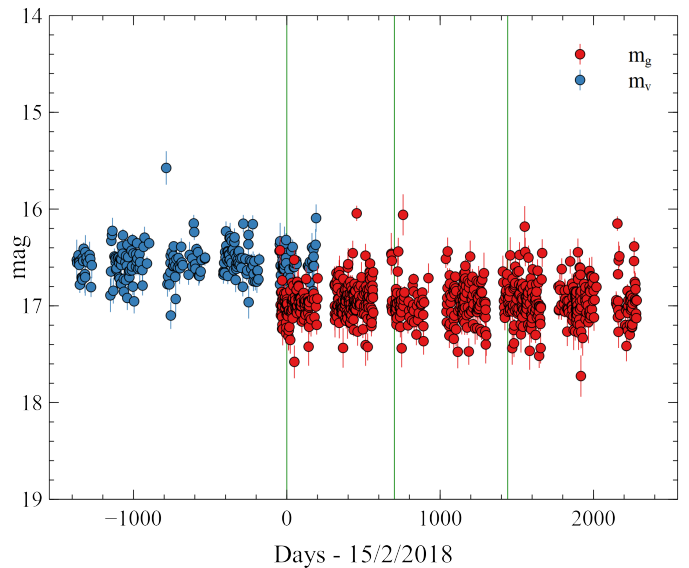
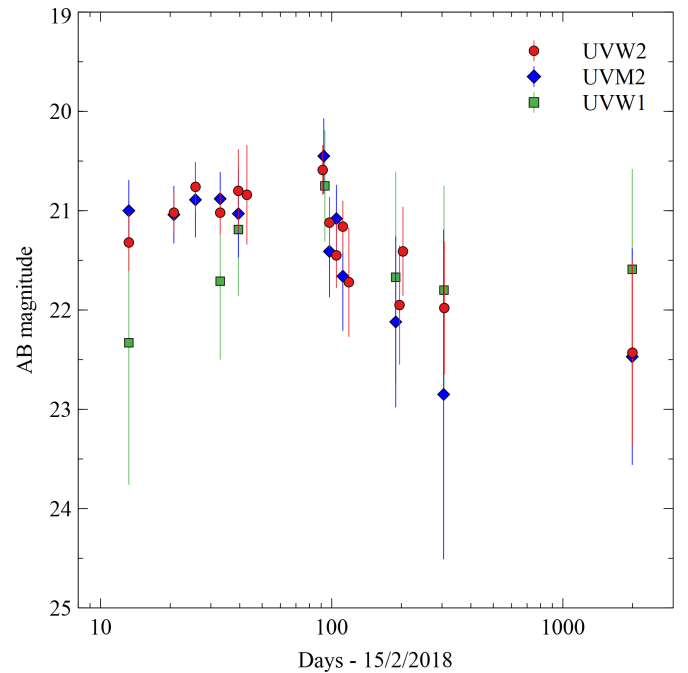


Fig. 4. Light curve of XMMSL2 J1404-2511 in the Swift-UV filters (upper) and in V and G filters from the ASAS-SN Sky Patrol v2.0 project (Hart et al. 2023; Shappee et al. 2014) (lower) where the vertical green lines indicate the dates of the three flares seen in X-ray data. Magnitudes represent the host galaxy light, which dominates in the optical filters, plus light from the TDE which dominates in the UV.

4. Radio observations

XMMSL2 J1404-2511 was observed with NSF's Karl G Jansky Very Large Array (VLA) at a mean frequency of 6 GHz on 2018 March 23 and again on 2018 September 8 under program 18A-453 (PI: Alexander). In the first observation the VLA was in its highest resolution A configuration, while in the second it was in its lowest resolution D configuration. Both observations used 3C286 as the flux calibrator and J1409-2657 as the phase calibrator and the data were reduced in CASA following standard procedures.

XMMSL2 J1404-2511 was not detected in either observation, with 3σ limits of $14 \mu\text{Jy}$ and $35 \mu\text{Jy}$ respectively.

¹ Using an alternative scaling relation (Greene et al. 2020) gives a consistent mass of $\log_{10}(M_{\text{BH}}) = 6.80 \pm 0.55 M_{\odot}$.

² <http://gsaweb.ast.cam.ac.uk/alerts/alertsindex>

Table 1. Swift-UVOT observations of XMMSL2 J1404-2511

Date	U	UVW1	UVM2	UVW2
13	20.93 ± 0.76	21.62 ± 0.69	20.80 ± 0.24	21.18 ± 0.23
21	21.01 ± 0.78	21.97 ± 0.87	20.84 ± 0.22	20.91 ± 0.18
26	21.73 ± 2.09	22.85 ± 2.80	20.72 ± 0.31	20.68 ± 0.22
33	-	21.25 ± 0.48	20.71 ± 0.21	20.92 ± 0.19
39	-	20.89 ± 0.49	20.83 ± 0.35	20.71 ± 0.38
43	19.95 ± 0.73	21.53 ± 1.53	21.74 ± 1.27	20.75 ± 0.46
51	-	21.07 ± 0.84	22.08 ± 1.37	22.55 ± 1.59
92	20.79 ± 1.09	20.54 ± 0.45	20.33 ± 0.34	20.52 ± 0.23
98	21.74 ± 1.75	21.55 ± 0.70	21.13 ± 0.33	21.01 ± 0.22
105	-	21.62 ± 0.76	20.87 ± 0.27	21.29 ± 0.27
112	22.44 ± 3.19	-	21.33 ± 0.38	21.04 ± 0.21
119	21.09 ± 1.40	21.47 ± 0.97	21.22 ± 0.66	21.52 ± 0.44
189	-	21.23 ± 0.68	21.64 ± 0.52	22.64 ± 0.97
196	21.06 ± 1.14	21.88 ± 1.16	22.34 ± 0.99	21.72 ± 0.45
203	20.49 ± 0.75	-	-	21.26 ± 0.38
208	-	-	21.66 ± 1.11	21.45 ± 0.85
306	-	21.31 ± 0.64	22.06 ± 0.74	21.74 ± 0.51
1989	-	21.46 ± 0.81	22.54 ± 1.02	22.34 ± 0.87
1995	20.72 ± 1.05	21.17 ± 0.66	21.86 ± 0.57	22.06 ± 0.69
1999	-	-	22.26 ± 0.68	22.08 ± 0.65
2301	-	-	-	21.87 ± 0.36
2309	-	-	-	22.34 ± 0.61
2319	-	-	-	21.23 ± 1.11

Notes. Swift-UVOT host-subtracted, Galactic-extinction corrected AB magnitudes. Date specifies the number of days since 15/02/2018.

5. X-ray observations and long-term light curve

After discovery, a monitoring program was immediately initiated with *Swift* with a cadence of one observation per week. Despite being discovered in an XMM-Newton slew the source had formally left the XMM-Newton visibility window at the time and could only be observed by XMM-Newton, in a pointed observation, five months later (OBSID=0804860201). A second pointed observation was made after a further six months (OBSID=0804860301). The full list of X-ray observations is given in Tab. 2.

Swift spectral products were extracted using the on-line XRT data products tool available from the UK Swift Data centre (Evans et al. 2009). As another source lies at ~ 1 arcminute from XMMSL2 J1404-2511 we entered the source coordinates for the fainter observations to avoid problems with the centroiding routine. A brief analysis of the secondary source spectrum is presented in Appendix A.

Data from the first XMM-Newton observation were reduced using SAS 18.0 (Gabriel et al. 2004). Source products were extracted from a circle of radius 27 arcseconds about the source and a local background was taken from the same CCD. The background was low throughout the observation and flare screening was not applied. We restricted our analysis to the EPIC-pn camera.

The long-term 0.2-2 keV observed flux light curve is given in Fig. 5 and can be characterised by a flat flux level for the first 100 days followed by a decay of $t^{-5.2 \pm 0.2}$. A similar 100-day initial flat period followed by a constant decay was seen in XMMSL1 J1446+68 (Saxton et al. 2019), although the rate of decline is considerably steeper in XMMSL2 J1404-2511, of the order of a factor 500 in 230 days. This decay is notably faster than observed in most previous events (Auchettl et al. 2017) including ASSASN-14li (Brown et al. 2017; Wen et al. 2020).

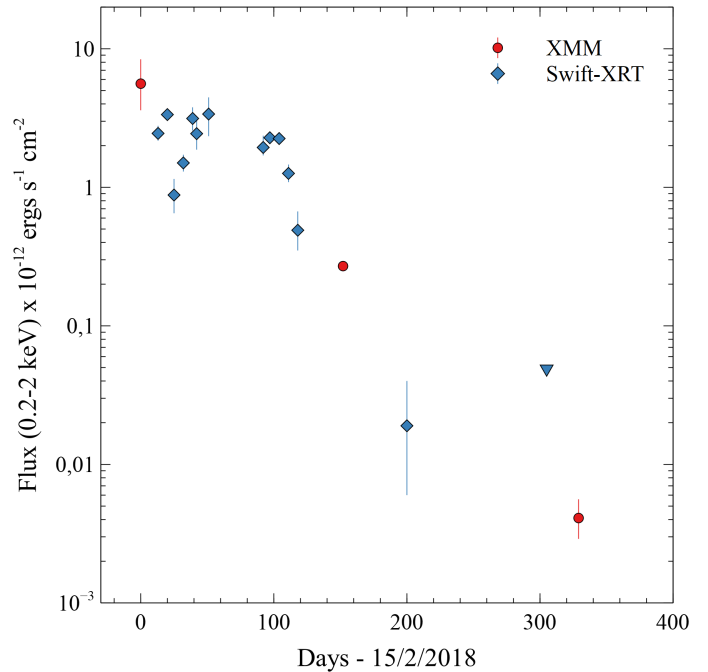


Fig. 5. Observed soft X-ray (0.2-2 keV) flux light curve of XMMSL2 J1404-2511 during 2018 and 2019. XMM-Newton points are shown as red circles and Swift-XRT points as blue diamonds or a blue downward triangle for the upper limit. Fluxes have been calculated using the spectral model *COMPBB* (see Tab. 3).

5.1. X-ray spectral analysis

The early Swift-XRT observations of 2018-02-28 and 2018-03-07 can be well fit with a single black-body model of temperature $kT \sim 80$ eV, absorbed by the Galactic column of $N_H = 6.7 \times 10^{20} \text{ cm}^{-2}$. TDEs at the peak of their emission commonly show a similar thermal spectrum (Komossa & Bade 1999; Esquej et al. 2008; Brown et al. 2017; Guolo et al. 2024). However, in subsequent observations the spectrum of XMMSL2 J1404-2511 hardened and became more complex. As an illustration, in Fig. 6 we show the evolution of the Swift-XRT spectrum between the observations of 2018-02-28 and 2018-03-19, where the hardening is very evident. To visualise the evolution of the spectrum, we parameterise the hardness of the X-ray spectrum over the full range of observations by the slope returned in a simple fit of a power-law, absorbed by the Galactic column, to the 0.3-10 keV spectra from XMM-Newton and Swift-XRT (Fig. 7). This model does not give a particularly good fit but clearly illustrates the evolution as the spectral index drops from $\Gamma \sim 5.5$, twenty days after discovery, to a minimum of $\Gamma < 3$ on days 100–120. Alternatively, we can parameterise the spectral hardness by fitting a single absorbed black-body to the same spectra (Fig. 7). The temperature of the black-body apparently increases from ~ 80 eV until it peaks at ~ 200 eV between days 100–120, in parallel with the changes seen in the power-law slope. We will see later that this does not represent the real temperature of the disc emission and point out here that care must be taken when interpreting measured X-ray temperatures in terms of real-world parameters, especially in low s/n spectra. In both parameterisations, the three observations taken between days 150 and 329 (X1,S13-16,X2) show tentative evidence for a softening of the

Table 2. X-ray observation log of XMMSL2 J1404-2511

Mission	Key ^a	Date	Expos (s)	Count rate ^b
ROSAT	R1	1991-01-07	320	< 0.033
XMM slew	XS1	2018-02-15	3.4	4.4 ± 1.1
Swift-XRT	S1	2018-02-28	2856	0.084 ± 0.006
Swift-XRT	S2	2018-03-07	3157	0.124 ± 0.007
Swift-XRT	S3	2018-03-12	1394	0.033 ± 0.007
Swift-XRT	S4	2018-03-19	3064	0.066 ± 0.006
Swift-XRT	S5	2018-03-26	950	0.16 ± 0.02
Swift-XRT	S6	2018-03-29	436	0.10 ± 0.02
Swift-XRT	S7	2018-04-07	682	0.11 ± 0.02
Swift-XRT	S8	2018-05-18	1148	0.084 ± 0.010
Swift-XRT	S9	2018-05-23	2788	0.096 ± 0.007
Swift-XRT	S10	2018-05-30	2883	0.104 ± 0.007
Swift-XRT	S11	2018-06-06	2928	0.060 ± 0.005
Swift-XRT	S12	2018-06-13	1427	0.023 ± 0.005
XMM pnt	X1	2018-07-17	32900	0.217 ± 0.003
Swift-XRT	S13-16 ^c	2018-09-02	8064	$6.5 \pm 3.3 \times 10^{-4}$
Swift-XRT	S17	2018-12-17	2788	< 0.0020
XMM pnt	X2	2019-01-10	29874	$3.5 \pm 0.7 \times 10^{-3}$
NuSTAR	N1	2019-01-10	68557	< 0.0024 ^d
XMM slew	XS2	2020-07-17	2.1	< 1.72
eROSITA	eRASS1	2020-01-26	321	0.23 ± 0.03^e
eROSITA	eRASS2	2020-07-28	320	0.09 ± 0.02
eROSITA	eRASS3	2021-01-20	222	< 0.02
eROSITA	eRASS4	2021-07-28	219	< 0.04
eROSITA	eRASS5	2022-01-26	232	0.25 ± 0.03
Swift-XRT	S18-21 ^f	2023-08-02	9991	< 0.00043
Swift-XRT	S22-23 ^g	2024-06-07	2420	< 0.0012

^a R=ROSAT survey, XS=XMM-Newton slew, S=Swift-XRT, X=XMM-Newton pointed, N=NuSTAR, eRASS=eROSITA survey.

^b Detector count rate (counts/s) in the 0.2–2 keV energy band. Upper limits are 2σ .

^c Summation of 4 observations made on 2018-08-23, 2018-08-30, 2018-09-06 and 2018-09-11.

^d Upper limit to the count rate from the combined FPA and FPB NuSTAR detectors in the energy band 3–20 keV.

^e All eROSITA count rates and upper limits are background subtracted but have not been corrected for vignetting or encircled energy effects.

^f Summation of 4 observations made on 2023-07-28, 2023-08-02, 2023-08-03, 2023-08-07.

^g Summation of 2 observations made on 2024-06-04 and 2024-06-11.

spectrum; this is most obvious in the simple power-law fit where the slope steepens from 2.8 (in S12) to 3.6 (in X1).

A visual inspection of Fig. 6 shows that the flux below 0.7 keV declined between 2018-02-28 and 2018-03-19, while the flux above 0.7 keV increased. This immediately suggests that the soft photons have been reprocessed into harder photons.

We used the high-statistic XMM-Newton observation of 2018-07-17 (day 150), using the EPIC-pn data, grouped to have a minimum of 25 counts in each spectral bin, to investigate the spectral model. Spectral fits were performed with *XSPEC v12.13.1* (Arnaud 1996). All fits include absorption by the Galactic column ($N_H = 6.7 \times 10^{20} \text{ cm}^{-2}$) with Wilms abundances (Wilms et al. 2000).

First we tried single models, finding a poor fit with an absorbed black-body ($\chi_r^2 = 546/146$), bremsstrahlung ($\chi_r^2 = 251/146$) or a multi-colour disc (DISKBB model; $\chi_r^2 = 392/146$). A power-law proved a better fit ($\chi_r^2 = 166/146$, with $\Gamma = 3.63 \pm 0.05$). A good fit ($\chi_r^2 = 147/144$) was given by a black-body Comptonised by a warm electron pop-

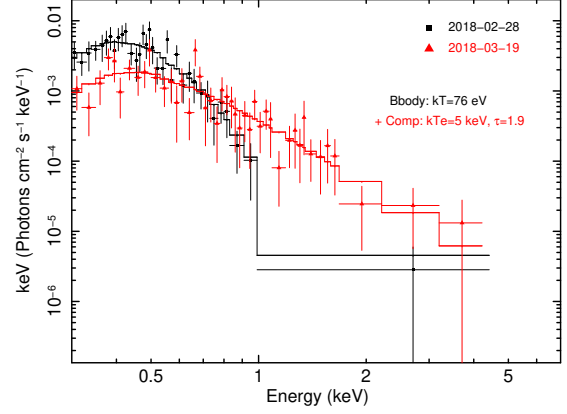


Fig. 6. Swift-XRT spectra of XMMSL2 J1404-2511 from 2018-02-28 fitted with a black-body (black) and 2019-03-19 fitted with a COMPBB model (red).

ulation (COMPBB; Nishimura et al. 1986) with a rest-frame black-body temperature of $kT = 48^{+16}_{-10}$ eV, electron temperature $kT_e = 2.7^{+6.2}_{-2.4}$ keV, optical depth $\tau = 3.8^{+1.3}_{-2.3}$ and normalisation of 5.3×10^4 . This model treats soft X-ray photons Compton-scattered by a plane-parallel plasma. Switching to a different comptonisation model (THCOMP; Zdziarski et al. 2020) gave a similar quality fit with comparable temperatures and optical depth.

As a further check we added an extra component of intrinsic cold absorption (*ztbabs*), at the redshift of the source, finding no improvement in the fit ($\chi_r^2 = 147/143$; $N_H < 1.5 \times 10^{20} \text{ cm}^{-2}$). A warm absorber (*absori*; Done et al. 1992; Magdziarz & Zdziarski 1995) likewise gave no significant improvement ($\chi_r^2 = 147/142$).

We then applied the *COMPBB* model to the lower-statistic Swift-XRT observations, fixing the electron temperature to $kT_e = 5$ keV. We choose this temperature as being close to the centre of the allowed range from the XMM-Newton observation and note that it is hotter than the 0.1–1.0 keV temperature derived for the soft excess in a sample of AGN (Petrucci et al. 2018) but well below the temperature of the hot corona (e.g. Akylas & Georgantopoulos 2021). Results are presented in table 3. The evolution of the optical depth of the electron corona is shown in Fig. 7 and jumps from $\tau < 0.4$ to an optical depth $\tau > 1.6$ in 12 days between 2018-02-28 and 2018-03-12 or from $\tau = 0.4 \pm 0.3$ to $\tau = 1.9^{+0.5}_{-0.3}$ in 5 days from 2018-03-07 to 2018-03-12. Overall the corona went from being undetectable to being fully formed, with a depth $\tau = 2.9 \pm 0.5$, in 29 days between 2018-02-28 and 2018-03-29.

Over the set of observations, the observed temperature of the disc emission dropped from ~ 80 eV in the early Swift observations to $kT = 50 \pm 10$ eV (with kT_e fixed at 5 keV) in the XMM-Newton observation of 2018-07-17 (Tab. 3).

As an alternative we investigated whether a high-temperature (fixed to 70 keV), low optical depth, Comptonisation model could also fit the X1 spectrum. Using the *COMPBB* model the fit is bad (267/145), but changing to the *COMPTT* model (Titarchuk 1994) does allow a reasonable high-temperature (frozen to 70 keV), $\tau = 0.015 \pm 0.003$ fit to the EPIC-pn data ($\chi_r^2 = 151/144$). As noted elsewhere (e.g. Akylas & Georgantopoulos 2021; Tamborra et al. 2018), extracting physical parameters for the electron population in the corona is very model dependent

unless a high-energy break is available to constrain the electron temperature.

To further probe the intrinsic disc parameters we used a physically-motivated disc model *TDEDISCSPEC* (Mummery 2021). This models the disc as the sum of emission from a set of concentric regions, each with their own temperature and area, and with the intrinsic emission colour-corrected to model disc effects such as opacity (Mummery et al. 2023). It has two main parameters; T_p , the intrinsic peak disc temperature before colour-correction effects are applied, and R_p , the disc radius where the peak temperature is emitted. We applied this model to the first *Swift*-XRT observation (S1), which is the only good-quality spectrum we have which is purely thermal. This fits the spectrum well ($C_r = 40/50$) giving a best-fit radius $R_p = 6.1^{+3.3}_{-1.5} \times 10^{11}$ cm and peak temperature $T_p = 6.5^{+1.0}_{-0.6} \times 10^5$ K (56^{+9}_{-5} eV), when we fix the index ($\gamma = 0.5$) and the luminosity distance to $D_L = 190$ Mpc. For the second *Swift*-XRT observation (S2), to model the Comptonisation we adopted the *SIMPL* model (Steiner et al. 2009), which links an arbitrary seed spectrum to an output power-law. This has three parameters, a power-law slope Γ , the fraction of seed photons which are scattered f_c and a flag which we set so that only upscattering of photons is considered. This gave a similar quality fit to the *COMPBB* model with $C_r = 89/65$, $R_p = 5.4^{+1.5}_{-1.2} \times 10^{11}$ cm and peak temperature $T_p = 7.3^{+0.6}_{-0.6} \times 10^5$ K and $f_c < 0.05$. From observation S3 onwards the Comptonisation component becomes large and we find that fits with the *TBABS*SIMPL*TDEDISCSPEC* model return values of R_p and T_p which are unconstrained. A similar effect was noted by Guolo et al. (2024), who found that such fits become unreliable when $f_c > 0.2$.

To break the degeneracy we use the relation found in Mummery et al. (2023) between R_p and black hole mass, $R_{p,12} = M_{BH,6}/4.9$, where $R_{p,12}$ is the radius of the peak temperature in units of 10^{12} cm and $M_{BH,6}$ the mass of the black hole in units of $10^6 M_\odot$, to fix R_p . Using a variety of methods we estimate M_{BH} for 2MASX 1404-25 to be $4 \pm 2 \times 10^6 M_\odot$ (see appendix B). From this we get $R_{p,12} = 0.82 \pm 0.41$. Fits were conducted, using these values of R_p and are given in Tab. 4.

5.2. Bolometric Lightcurve

The X-ray light curve does not run parallel with the bolometric light curve and X-ray decay rates can be exaggerated by the disc temperature declining as the luminosity falls. In fact the discrepancy becomes exponential as the temperature drops below that of the observed X-ray energy range (see figures 14 and 15 of Mummery et al. 2023). The work of Mummery et al. (2023) considered the correction (η_X) needed to convert between thermal X-ray and bolometric luminosity. This varies slowly for $kT \geq 50$ eV but rises exponentially as the temperature decreases. In section 5.1 we show that the spectrum of XMMSL2 J1404-2511 becomes modified by Compton up-scattering of disc photons. This will temper the dramatic variation of η_X as the luminosity and hence temperature of seed photons drops, due to lower energy photons being shifted into the X-ray band. As an example of this effect, in Fig. 8 we show $\eta_X \propto T_X$ for the Comptonisation model *COMPBB*, with electron temperature $kT_e = 2$ keV and optical depth fixed at $\tau = 2$ or $kT_e = 5$ keV and $\tau = 1$ (values which are permitted by the spectral fits of section 5.1).

We can estimate L_{bol} using fits of the Comptonised thermal disc spectrum (Tab. 4) to the X ray spectra. In bolometric light, the steep decay of the X-ray light curve starting from day 100, flattens to a decay index of $t^{-4.6 \pm 0.3}$ (Fig. 9).

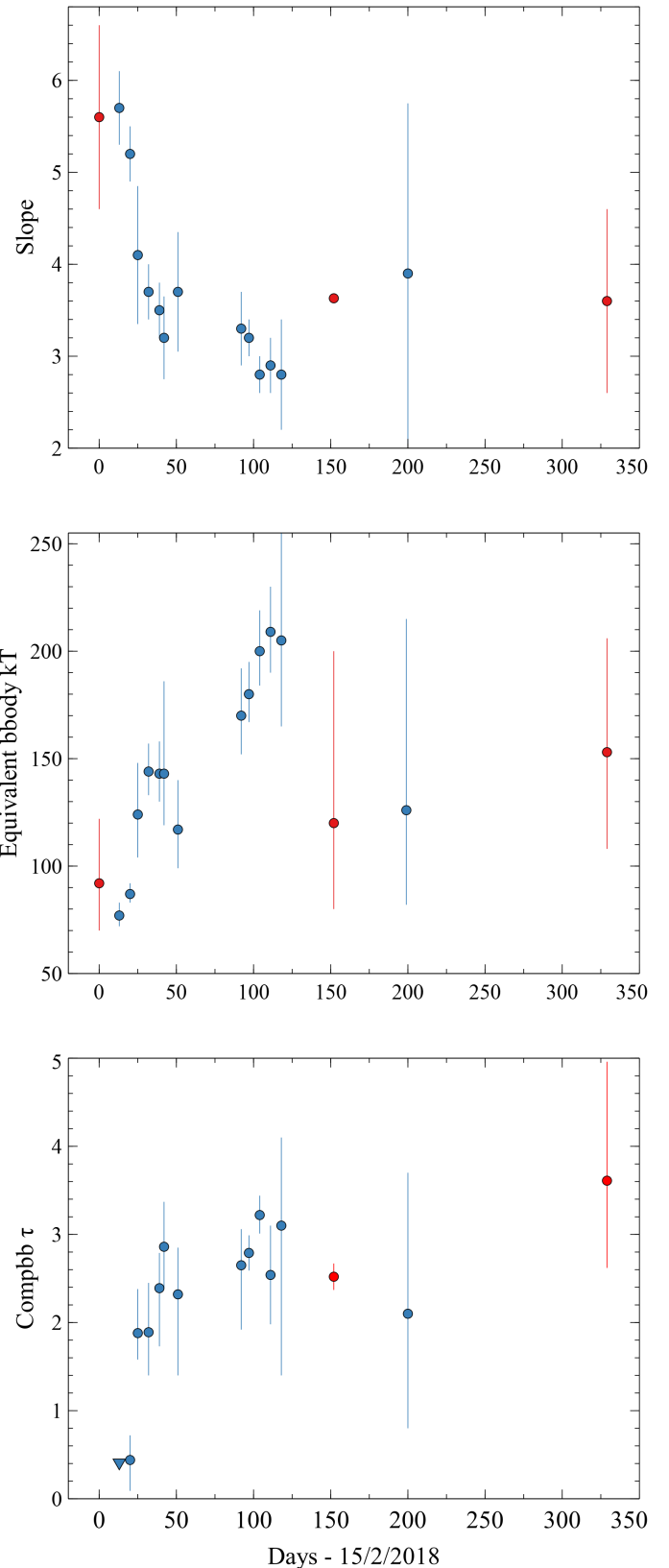


Fig. 7. Upper: Slope of a power-law model absorbed by the Galactic column fitted to the X-ray spectra of XMMSL2 J1404-2511. Red points are from XMM-Newton, blue points from Swift-XRT. Middle: Temperature (eV) of a simple model of a black-body absorbed by the Galactic column of $N_H = 6.7 \times 10^{20} \text{ cm}^{-2}$ fitted to the X-ray spectra of XMMSL2 J1404-2511. Note that this does not represent the physical temperature of the disc but illustrates how the spectrum hardens with time. Lower: Optical depth of a 5 keV electron population derived from fits of a *COMPBB* model, absorbed by the Galactic column, to X-ray spectra of XMMSL2 J1404-2511 from 2018 and 2019.

Table 3. Fits of a Comptonised black-body to XMM-Newton, Swift-XRT and SRG/eROSITA observations of 2MASX 1404-25

Date	Key	kT^a eV	τ^b	Flux (0.2–2 keV) $10^{-12} \text{ ergs s}^{-1} \text{ cm}^{-2}$	C/dof
2018-02-28	S1	76^{+6}_{-5}	< 0.41	$2.46^{+0.30}_{-0.29}$	39/50
2018-03-07	S2	80 ± 8	$0.44^{+0.28}_{-0.35}$	$3.36^{+0.31}_{-0.33}$	89/66
2018-03-12	S3	< 88	$1.88^{+0.30}_{-0.30}$	$0.99^{+0.31}_{-0.28}$	24/24
2018-03-19	S4	77^{+27}_{-46}	$1.89^{+0.36}_{-0.49}$	$1.50^{+0.23}_{-0.20}$	76/81
2018-03-26	S5	< 98	$2.39^{+0.40}_{-0.66}$	$3.20^{+0.65}_{-0.57}$	65/65
2018-03-29	S6	< 72	$2.86^{+0.51}_{-0.47}$	$2.48^{+0.75}_{-0.61}$	34/34
2018-04-07	S7	< 91	$2.32^{+0.53}_{-0.92}$	$3.51^{+1.01}_{-1.02}$	37/29
2018-05-18	S8	< 98	$2.65^{+0.41}_{-0.73}$	$1.98^{+0.42}_{-0.39}$	43/63
2018-05-23	S9	< 55	$2.79^{+0.20}_{-0.29}$	$2.28^{+0.28}_{-0.25}$	117/120
2018-05-30	S10	< 59	$3.22^{+0.20}_{-0.21}$	$2.25^{+0.26}_{-0.24}$	135/140
2018-06-06	S11	94^{+37}_{-50}	$2.54^{+0.56}_{-0.56}$	$1.20^{+0.18}_{-0.16}$	84/95
2018-06-13	S12	< 163	$3.1^{+1.0}_{-1.7}$	$0.49^{+0.19}_{-0.14}$	22/24
2018-07-17	X1	50^{+9}_{-10}	$2.52^{+0.15}_{-0.15}$	$0.27^{+0.01}_{-0.01}$	147/145
2018-09-02 ^c	S13-S16	50^d	$2.1^{+1.6}_{-1.3}$	$0.019^{+0.022}_{-0.013}$	4.8/5
2019-01-10	X2	50^d	$3.61^{+1.35}_{-0.99}$	$0.0042^{+0.0014}_{-0.0013}$	123/133
2020-01-26	eR1	50^d	$2.2^{+0.4}_{-0.2}$	$0.49^{+0.09}_{-0.10}$	50/55
2020-07-28	eR2	50^d	$3.8^{+1.2}_{-1.9}$	$0.17^{+0.05}_{-0.06}$	22/25
2022-01-26	eR5	50^d	$2.7^{+0.5}_{-0.7}$	$0.51^{+0.10}_{-0.12}$	41/45

Notes. Spectral fits to observations of 2MASX 1404-25, modelled by *TBABS*COMPBB*, consisting of a single-temperature black-body Comptonised by electrons with kT_e fixed at 5 keV, absorbed by the Galactic column of $N_H = 6.7 \times 10^{20} \text{ cm}^{-2}$. Fits used cstat statistics, quoted errors and upper limits are 90% confidence.

^(a) Observed black-body temperature returned by the fit. Note that this does not represent the physical temperature of the disc, whose emission can be better conceived as the sum of a set of black-bodies of different temperatures subject to multiple correction factors (Mummery 2021). ^(b) Optical depth of a 5 keV plasma. ^(c) Combination of observations S13–S16 (2018-08-23 – 2018-09-11). ^(d) Black-body temperature fixed to $kT = 50 \text{ eV}$.

From the XMM-Newton slew observation, the peak luminosity was $L_X = 6.5^{+3.2}_{-2.3} \times 10^{43} \text{ ergs s}^{-1}$ and applying the correction factor appropriate for a thermal model of $kT=92 \text{ eV}$ ($1 \times 10^6 \text{ K}$), $L_{\text{bol}} = 8.3^{+4.1}_{-3.0} \times 10^{43} \text{ ergs s}^{-1}$. The total luminosity integrated over the bolometric light curve is $5 \times 10^{50} \text{ ergs}$, equivalent to an accreted mass of $\sim 0.003 M_\odot$ during the 329 days of observations, for a mass to light conversion efficiency $\eta = 0.1$ (Gruzinov 1998). As the observations may have missed the peak of the emission this value is necessarily a lower limit.

5.3. NuSTAR observation

To help determine whether the steep flux decay starting around day 100, was intrinsic or could have been caused by local absorption, a 69 ks observation was made with NuSTAR (Harrison et al. 2013) under ObsID 90401640002 simultaneously with the second XMM-Newton pointed observation. The NuSTAR data were reduced by using the standard NuSTARDAS software v1.8.0 and CALDB 20170727. We used a circular extraction region with a radius of $25''$ centered on the coordinates of XMMSL2 J1404-2511 to extract any source counts. Background counts were extracted from a source free region in the same quadrant, using a circular region with a radius of $100''$. We used the same regions for both telescopes, FPMA and FPMB. The source was barely detected in the XMM-Newton soft (0.2–2 keV) band and was not detected at all with NuSTAR with an upper limit of $2.4 \times 10^{-3} \text{ c/s}$ from the combined FPMA and FPMB data in the 3–20 keV band, equating to a 2- σ upper limit of $F_X < 4.8 \times 10^{-14} \text{ ergs s}^{-1} \text{ cm}^{-2}$ in that band³ (Fig. 10). Using the combined XMM-Newton and NuSTAR spectrum we can set constraints on the level of absorp-

tion which would be needed to explain the drop in flux purely by intrinsic absorption in the vicinity of the source. If we fit that combined spectrum with the spectral parameters from the first XMM-Newton pointed observation then to get a good fit we would need to add a combination of a neutral absorber with $N_H = 3.5^{+2.5}_{-2.0} \times 10^{21} \text{ cm}^{-2}$ and an ionised absorber (ZXIPCF; Reeves et al. 2008) with $N_H = 3.8^{+2.4}_{-1.8} \times 10^{23} \text{ cm}^{-2}$ and ionisation parameter $\log \xi = 2.1^{+0.8}_{-0.2}$ both at the redshift of the source, yielding $C_r = 122/133$. A single absorber does not provide a good fit to the data.

5.4. eROSITA and late-time Swift observations

The position of XMMSL2 J1404-2511 was observed during five eROSITA (Predehl et al. 2021) all-sky surveys (eRASS) between 2020 and 2022. The eROSITA data were calibrated and cleaned using the pipeline version 020 of the eROSITA Science Analysis Software (eSASS, Brunner et al. 2022). For each eRASS, we merged all photon events from the seven telescopes into one event list file. The X-ray spectra and light curves for each eRASS were extracted using the srctool in eSASS (version 20211004). A circular region with a radius of $40''$ was chosen as the source region for all eRASSs. While a source-free annular region with an inner radius of $100''$ and an outer radius of $250''$ was selected as the background region.

XMMSL2 J1404-2511 was detected by eROSITA in eRASS1, 2 and 5 (Tab. 2) at fluxes above the low state of 2019-01-10. The full light curve is shown in Fig. 11, and although the monitoring is very sparse, the data are consistent with three roughly equally-spaced flares. This is very similar to the long-term light curve of eRASS J045650.3-203750, which showed multiple flares interpreted as repeated partial disruptions of a stellar object (Liu et al. 2023, 2024). A suggested three-

³ Calculated using a source circle of radius $29''$ (containing 50% of the counts; Harrison et al. 2013), a local background and a spectrum of a power-law of $\Gamma = 3.4$ absorbed by the Galactic column.

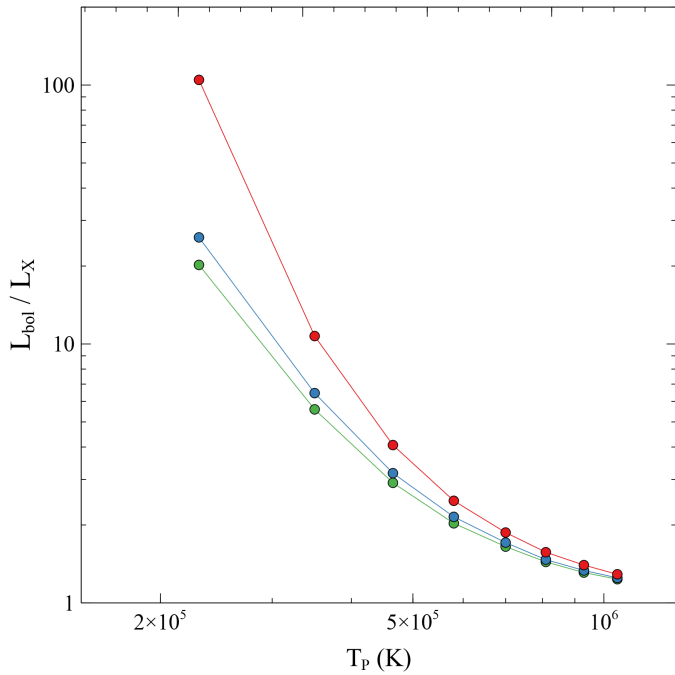


Fig. 8. Bolometric correction factor for 0.2–2 keV emission from a single temperature thermal spectrum (red) and a Comptonised thermal spectrum with electrons of temperature 2 keV and $\tau = 2$ (blue) and 5 keV with $\tau = 1$ (green), plotted against the peak temperature of the thermal component.

tally destroyed. Future X-ray observations around February 2026 should be able to confirm this.

6. Discussion

From the lack of broad and narrow emission lines in the optical spectrum, the initially purely thermal X-ray spectrum and the very low luminosity of the second XMM-Newton pointed observation, we strongly disfavour AGN activity. The Wise colours, $W1=13.476$ mag (Vega), $W2=13.445$ mag (Vega) also support the classification of 2MASX 14044671-2511433 as a non-active galaxy (Stern et al. 2012). Therefore, we ascribe the observations of XMMSL2 J1404-2511 to a new accretion event, i.e. a TDE. The optical/UV characteristics of XMMSL2 J1404-2511 are similar to many other TDEs, given the rather poor monitoring data that we have, i.e. a standard temperature of a few $\times 10^4$ K and a slow decay. However, the long-term ASAS-SN light curve does not show an optical peak at any stage (Fig. 4), which is unusual for a TDE⁴. Point to point variations in the V-band light curve yield an upper limit of 3×10^{42} ergs s⁻¹ for any possible optical peak prior to the X-ray discovery. Optical emission from XMMSL2 J1404-2511 is most easily understood as emission from the outer regions of the accretion disc (e.g. Mummery & Balbus 2020; Mummery & van Velzen 2024; Guolo & Mummery 2025).

We can then attempt to interpret the observations in terms of a TDE model capable of addressing the distinctive X-ray characteristics of XMMSL2 J1404-2511: 1. A plateau of at least 100 days. 2. The development of a harder component on a timescale of ~ 10 days. 3. A steep decay of the X-ray flare by a factor

⁴ Although an increasing number of X-ray discovered TDEs are being found with no simultaneous or preceding optical transient (Sazonov et al. 2021; Jin et al. 2025).

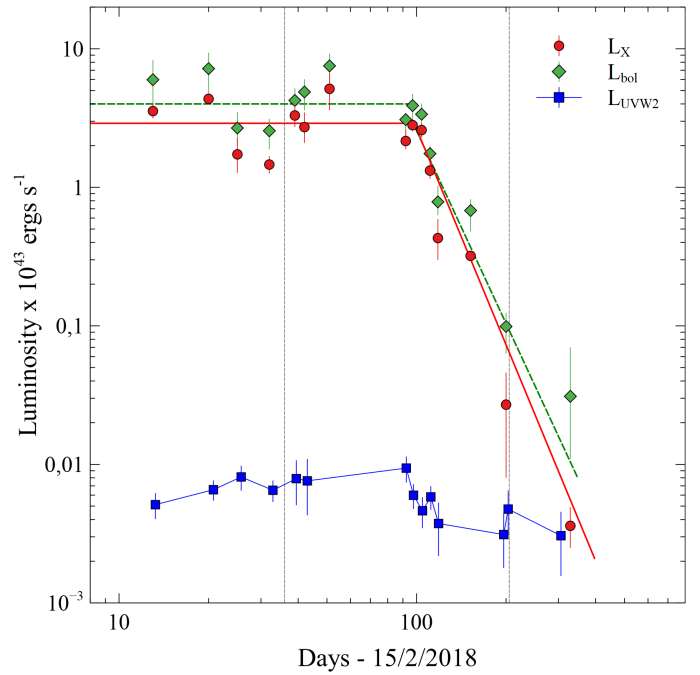


Fig. 9. X-ray (red circles), host-subtracted, absorption-corrected, UVOT-UVW2 filter (blue squares) and bolometric (green diamonds) luminosity light curves. Bolometric luminosities have been calculated from fits of a Comptonised thermal disc model to the X-ray spectra (see section 5.1). Solid red line gives a fit of constant flux in the early phase and a decay of $t^{-5.2}$ from day 100 to the X-ray luminosity. Dashed green line gives the same for the bolometric luminosity with a decay of $t^{-4.6}$. Grey vertical dashed lines indicate the times of the radio non-detections.

~ 500 over ~ 200 days after the end of the plateau. 4. Repeated flares in later data.

6.1. X-ray light-curve plateau

The first TDEs discovered by ROSAT showed sharp decays in their light curves interpreted as a response to a reduction in the rate of returning debris (Komossa 2004, and references therein). As can be seen from Fig. 9, the X-ray flux, and the inferred bolometric flux in XMMSL2 J1404-2511 vary little over the first 100 days of observations. We interpret this as a plateau similar to that seen in several sources such as XMMSL2 J144605.0+685735 (Saxton et al. 2019) and ASSASN-150i (Gezari et al. 2017). The lack of previous X-ray observations prevent us from knowing the full duration of the plateau⁵. There are two main reasons why the light curve might decay more slowly than the rate of incoming material. When the fall back rate is super-Eddington, a combination of energy advected into the black hole (photon trapping) (Abramowicz et al. 1988; Ohsuga et al. 2002), increasing colour-correction factor (Wen et al. 2020) and loss of material in high-speed winds (e.g. Dai et al. 2018) leads to a self-limiting emitted X-ray luminosity, which has been used to explain the flat light curve of 3XMM J150052.0+015452 (Lin et al. 2017; Cao et al. 2023). The fact that an accretion disc state change (i.e. development of a hard component), which is expected to happen at sub-Eddington accretion rates (Esin et al. 1997; Maccarone

⁵ We note that had the Einstein Probe (Yuan et al. 2016) been in nominal operations prior to 2018, the question of previous behaviour would have been resolved, illustrating what a great asset that mission will be to TDE astronomy.

2003, and see Section 6.3), occurred in XMMSL2 J1404-2511 during the plateau phase argues against a sustained period of super-Eddington accretion during the plateau in this case.

A more likely explanation is that debris spreads out into an accretion disc which accretes viscously (Cannizzo et al. 1990; Mummery & Balbus 2020; Jonker et al. 2020). If this happens then the disc can act as a reservoir of accretable material until the rate of incoming debris falls below the rate of material being consumed centrally, in which case the luminosity will drop again.

The UV/optical luminosity during the plateau is lower than seen in many TDEs, with a mean plateau luminosity in the UVOT-U filter of $L_U \sim 5 \times 10^{40}$ ergs s⁻¹. From the relationship between optical plateau luminosity and black hole mass derived in Mummery et al. (2024) we obtain a mass of $3.5^{+3.5}_{-1.7} \times 10^5 M_\odot$. This is lower than our other estimates (Appendix B), but we note that the scatter of the Mummery et al. (2024) relationship is particularly large at the low mass end, while being constrained at the other end by the Hills mass.

6.2. What triggers the development of the corona and when does it happen?

At the time of the development of the Comptonisation zone the observed temperature of the disc emission was $kT \sim 80$ eV. If we take 2018-03-07 as the date when the zone formed then, from Tab. 4, the bolometric luminosity was $L_{\text{bol}} = 7 \pm 3 \times 10^{43}$ ergs s⁻¹ and the Eddington ratio $0.13^{+0.14}_{-0.04}$ for the adopted mass of $M_{\text{BH}} = 4 \pm 2 \times 10^6 M_\odot$. From Mummery et al. (2023) we see that disc orientation can increase the bolometric correction, and hence implied accretion rate, at this temperature by up to a factor 4 due to the X-ray emitting region being obscured by the outer disc. The absence of intrinsic absorption in the X-ray spectrum makes it unlikely that we are seeing the emission at very high inclination angles so this effect is likely to be moderate; this argument could be made yet more strongly for AT2021ehb by Yao et al. (2022) where the disc was thicker.

State transitions are commonly seen in accreting Galactic black hole binaries (Belloni et al. 1997; Remillard & McClintock 2006). Changes on timescales of days or longer in these systems have been attributed to disc instabilities (e.g. Dubus et al. 2001; Kalemci et al. 2013), which when scaled up to the size of SMBH are far longer than those seen here. However, in specific binaries that show signs of obscuration and are accreting near the Eddington limit (such as GRS 1915+105, V4641 Sgr, V404 Cyg), analogous spectral transitions can occur within about 10 seconds (Rao et al. 2000; Maitra & Bailyn 2006; Kajava et al. 2020). If scaled linearly from a $10 M_\odot$ to a $10^6 M_\odot$ SMBH, these rapid viscous time-scale spectral transitions would imply a state change of 10^6 seconds (~ 10 days), totally consistent with that seen in XMMSL2 J1404-2511. Destruction and construction of an X-ray corona, possibly associated with a tidal disruption event, has also been seen to occur on a timescale of 10s to 100 days in a changing-look AGN (Ricci et al. 2020; Li et al. 2024). Finally it is interesting to compare this event with the still faster quasi-periodic eruptions (QPEs Miniutti et al. 2019; Giustini et al. 2020; Arcodia et al. 2021) seen in other TDE systems. The spectral change in XMMSL2 J1404-2511 is superficially similar to that seen in e.g. GSN069, where the effective temperature of the emission increased from 50 eV to 120 eV. In GSN069 this change occurs in 2000-3000 seconds (Miniutti et al. 2019), several hundred times faster than in XMMSL2 J1404-2511.

From Fig. 7 it takes 12 days to increase the effective temperature to 120 eV. Even considering the lightest possible black hole in GSN 069 allowed by the M-sigma relation of $3.2 \times 10^5 M_\odot$ (Wevers et al. 2022), scaling down linearly would still need ~ 1 day for the change, a factor 50 slower than the QPEs. Hence it seems unlikely that the same mechanism is responsible for the spectral changes seen in both XMMSL2 J1404-2511 and QPEs.

When the corona in XMMSL2 J1404-2511 begins to form there is a coincident drop and recovery in flux (Fig. 12) equivalent to a loss in total bolometric luminosity of $\sim 10^{49}$ ergs or accretion energy of $\sim 10^{50}$ ergs, assuming a mass to light conversion factor of 0.1. If the two are related then this may suggest that accretion energy is temporarily redirected into the creation of the warm corona, e.g. by magnetically heating the outer skin of the disc (Gronkiewicz & Różańska 2020), or into increasing its optical depth. Our observations show a timescale for the creation of the warm corona around a $M_{\text{BH}} \sim 10^6 M_\odot$ black hole of ~ 10 days which models will need to comply with. Similar model constraints for a transition in the opposite direction are provided by the destruction, or at least significant reduction, of the hot corona in ~ 3 days in AT2021ehb (Yao et al. 2022).

6.3. Why is corona creation in TDEs not ubiquitous?

Guolo et al. (2024) looked at X-ray data from optically-discovered TDEs, finding that at least 40% had X-ray emission and showing that the perceived preponderance of optical TDEs (Gezari 2021; Hammerstein et al. 2023) is strongly biased by the current superiority of optical surveys in identifying TDEs. Only 3 of the 17 optically-selected, X-ray detected TDEs were seen to develop a hard X-ray corona. Conversely, from a literature search we find that 10 of the 12 TDEs and candidate TDEs discovered in the XMM-Newton slew survey had or subsequently developed a significant hard component on top of the thermal disc emission in at least one observation⁶ (Tab. 5). A Monte Carlo simulation ran 100,000 times gives a probability of 0.04% that the XMM slew and optically-selected sets are drawn from the same population. If we remove from the slew sample the TDEs which showed evidence of a possible pre-existing AGN then the ratio becomes 6 out of 7 and the probability 0.14%. On the face of it this suggests that there is an intrinsic difference between optically and X-ray identified TDEs and that observed differences are not purely due to viewing angle (Dai et al. 2018; Gezari 2021). However, as pointed out in Guolo et al. (2024) and evident from Fig. 8, TDEs which develop a hard component become more luminous in X-rays, making them more likely to be detected in time-limited X-ray surveys such as the XMM-Newton slew survey⁷. More importantly, monitoring campaigns of events need to extend into epochs when the hard component becomes detectable. We note that two of the thermal TDEs from the Guolo et al. (2024) sample, AT2019teq (Yao & Guolo 2022; Ajay et al. 2022) and ASASSN-15oi (Hajela et al. 2025) have recently developed a hard X-ray corona. Further monitoring of the optical sample is therefore needed to confirm whether the apparent discrepancy in coronal properties is real.

⁶ Curiously the two XMM-Newton slew TDE which are purely or mainly thermal are the only ones which exhibit QPEs (Miniutti et al. 2019; Chakraborty et al. 2021). This may be related to the fact that QPEs, by their nature, are more easily detected as enhancements on top of very soft X-ray spectra but it does open the possibility that the mechanism responsible for QPEs is present in many TDEs.

⁷ Note that this will also be true for the eROSITA survey (Sazonov et al. 2021) and to some extent, flux-limited surveys like the Einstein Probe (Yuan et al. 2016).

Wevers (2020) proposed that the transition to a harder state occurs in TDEs when the accretion rate drops below a value of $f_{edd} \sim 10^{-2} - 10^{-1} L_{edd}$, finding that TDEs in the X-ray thermal state were more luminous than those displaying coronal emission ("Fainter harder brighter softer"). AT2021ehb and AT2020ocn, however, failed to show a simple connection between the accretion rate and X-ray hardness ratio (Guolo et al. 2024). In XMMSL2 J1404-2511 we find that the state change appears at $f_{edd} \sim 0.1 L_{edd}$.

We will consider three separate components while discussing the observed spectra: a thermal component from the disc, a hot, optically-thin electron corona indicated by a power-law component with a slope less than 2.5 and a warm, optically-thick, electron corona, indicated by a power-law with a slope of 2.5 or more. Compton upscattering of photons from a warm corona, consisting of an electron population with $kT_e \sim 0.1 - 1$ keV and optical depth $\tau > 1$ has been argued to be responsible for the characteristic shape of the X-ray soft-excess in many AGN (Magdziarz et al. 1998; Done et al. 2012; Petrucci et al. 2018; Ballantyne et al. 2024; Palit et al. 2024). It is envisaged as either an extra optically-thick layer on top of the standard accretion disc (Janiuk et al. 2001; Gronkiewicz et al. 2023) or a radial structure separated from the disc (Done et al. 2012; Kubota & Done 2018). In AGN the slope of the hot coronal power law is almost always below 2.5 (Ballantyne et al. 2024) except in NLS1 when they are accreting at very high rates (Ojha et al. 2020; Grünwald et al. 2023). We take the hot and warm coronae to be separate physical components as justified for example by time delays seen between energy bands (e.g. Gallo et al. 2004). Indeed, Liu et al. (2023) recover both a hard power-law and a soft-excess component in the repeating partial TDE, eRASSt J045650.3-203750.

Warm coronae in AGN are found with electron temperatures between 0.1 and 1 keV (Petrucci et al. 2018) and optical depths of 10–20 (Petrucci et al. 2018; Ballantyne et al. 2024). In XMMSL2 J1404-2511 we find $kT_e = 2.7^{+6.2}_{-2.4}$ keV and $\tau \sim 3$. Similar values were found in observations of the TDEs AT2020ocn ($kT_e = 2.4^{+1.4}_{-0.7}$, Cao et al. 2024) and 3XMM J150052.0+015452 ($2.3^{+2.7}_{-0.8}$, Cao et al. 2023), although in other observations of AT2020ocn (Cao et al. 2024) and in eRASSt J045650.3-203750 (Liu et al. 2023) electron temperatures < 1 keV, more typical of AGN, were seen.

Some events show both thermal X-ray and warm corona emission, e.g. eRASSt J045650.3-203750 (Liu et al. 2023) and AT2020ocn (Cao et al. 2024), who find that some spectra can be best fit with a patchy (i.e. covering factor < 1 corona). The lack of visible thermal emission in persistent AGN suggests that the covering factor is always 1 there, although we note that this can not be proven for AGN with higher mass black holes and hence cooler discs whose thermal emission does not reach the X-ray band. The only AGN which do show thermal X-ray emission are those which are believed to have experienced a recent TDE, e.g. 1ES 1927+654 (Ricci et al. 2020).

In summary, in some observations of TDEs the warm corona appears to be hotter, less optically thick and with a lower covering factor than the standard AGN soft excess.

The observed softening at late time of AT2021ehb and AT2018fyk (Yao et al. 2022; Wevers et al. 2023) can be explained by the reduction/disappearance of the hard power-law leaving the steeper-sloped soft excess dominant but not that the source has returned to the thermal state. Wevers et al. (2021) attribute the late-time softening of AT2018fyk to a transition into the quiescent state, which has parallels in X-ray binaries (Plotkin et al. 2013) and CLAGN (Ruan et al. 2019).

Table 5. TDEs discovered in the XMM-Newton slew survey

Name	Hard component?	Poss. AGN? ^a	References
NGC3599	yes	yes	(1)
2MASX 0740	yes	no	(2)
XMMSL1 1446+68	yes	no	(3)
XMMSL2 1404-25	yes	no	(4)
XMMSL1 1201+30	yes	no	(5)
XMMSL1 0619-65	yes	yes	(6)
SDSS J1323+4827	yes	no	(1)
NGC 5092	yes	yes	(7)
GSN 069 ^b	no	yes	(8)
XMMSL2 2030+04	yes	yes	(9)
MCG+07	yes	no	(9)
2MASX 0249 ^b	no	no	(1)

References. (1) Esquej et al. (2008); (2) Saxton et al. (2017); (3) Saxton et al. (2019); (4) This paper; (5) Saxton et al. (2012); (6) Saxton et al. (2014); (7) Li et al. (2020); (8) Miniutti et al. (2013); (9) Li et al. *in prep.*

^a Did the nucleus show optical emission lines indicative of a possible pre-existing AGN?

^b A power law component is ubiquitous in GSN 069 but has very low luminosity so that the corona, if present, is extremely weak. Chakraborty et al. (2021) did find a low-luminosity power-law component in 2MASX J0249 in an observation taken 16 years after discovery. However, the thermal component was still strongly dominant and so we consider this source to have not created a prominent corona to date.

6.4. Decay rate of the luminosity

At the end of the plateau phase, XMMSL2 J1404-2511 dropped in X-ray (bolometric) luminosity by a factor 500 (100) in 230 days, equivalent to a decay index of $t^{-5.2(-4.6)}$. This is much steeper than the canonical return of tidal debris ($t^{-5/3}$) (Rees 1988). It is also well in excess of the steeper decline of $t^{-9/4}$ predicted from partial disruptions (pTDE) where the stellar core survives (Coughlin & Nixon 2019; Nixon et al. 2021), although simulations show that a pTDE from a *weak* encounter can produce a decline in returning material with index up to 5 (Ryu et al. 2020).

Similar steep decays were seen in AT2018fyk (Wevers et al. 2021) whose X-ray luminosity fell by a factor 5000 in 170 days, eRASSt J045650.3-203750 with a factor 100 decay in a week (Liu et al. 2023) and RX J133157.6-324319.7 which exhibited a > 40 -fold decrease in 17 days (Malyali et al. 2023); all of these are repeating pTDEs (Wevers et al. 2023; Liu et al. 2023; Malyali et al. 2023). The implication is that the rapid drop to the quiescent state may have been caused by a deficit of available material in a small disc which was quickly consumed.

An even more abrupt decay in SWIFT J164449.3+573451 has been attributed to the turn-off of a relativistic jet due to the accretion rate falling below Eddington (Zauderer et al. 2013). The deep limits we present here on radio emission from XMMSL2 J1404-2511 (section 4) and the fact that the transition happened at an accretion rate well below Eddington make it unlikely that this is the responsible mechanism here.

The ultra-fast decline in the luminosity cycles of eRASSt J045650.3-203750 may have been augmented by a change of accretion disc state (Liu et al. 2023). Other sharp declines in AT 2019avd (Wang et al. 2024) which fell by a factor ~ 100 in ~ 50 days while the X-ray spectrum hardened and AT2021ehb, which dropped by a factor 10 in flux over 3 days,

accompanied by a softening of the X-ray spectrum, reinforce the idea of a transition to a less radiatively-efficient disc state accelerating the decline.

The discovery of more flaring activity by eROSITA (Fig. 11) leads to a viable interpretation for the rapid decay in the light curve of XMMSL2 J1404-2511, during 2018 and 2019, as being due to a partial disruption transferring a small quantity of material into an accretion disc. The fall in luminosity perhaps being accelerated by the disc transiting into a less radiatively-efficient state (Shen & Matzner 2014), when the accretion rate fell below a few % of Eddington.

We note that an alternative explanation for the repeated flares could be given by thermal instabilities in a disc fed by a single disruption event (Shen & Matzner 2014; Saxton et al. 2015; Piro & Mockler 2025). Models suggest that these can occur on timescales of months to a few years (Shen & Matzner 2014; Piro & Mockler 2025; Linial & Metzger 2024), compatible with the light curves seen in pTDEs to date.

In summary the XMMSL2 J1404-2511 data are consistent with a TDE discovered in the plateau phase, with X-ray and UV emission dominated by thermal emission from the disc. The conditions in the accretion structure were such that a corona quickly formed but faded away between days 100 and 300. The rapid decay of the X-ray flux in this event indicates a relatively small total amount of accreted mass and the repeat flares seen in the eROSITA data make it probable that the event consists of a series of repeated partial tidal disruptions. We note that we were fortunate to have the eROSITA survey to confirm the secondary flares which would otherwise have gone unnoticed. To avoid this in future, any TDE which shows an unusually rapid decay should be followed sporadically for several years after the event to check for repeat flares.

7. Conclusions

We identify the XMM-Newton slew transient, XMMSL2 J1404-2511, as a TDE which showed an unusually rapid flux and spectral evolution. The X-ray spectrum evolved from a low-temperature ($kT \sim 80$ eV) purely thermal spectrum to having a significant hard component within $< 5 - 12$ days, putting the strongest constraint to date on this disc state transition. After a plateau period of ~ 100 days, the X-ray luminosity decayed by a factor 500 over the following 230 days. We note that other sources with a similarly rapid decay also displayed evidence of a powerful corona and suggest that the accelerated evolution of these events is due to a partial tidal disruption, leading to a rapid decrease in available fuel and passage through different accretion disc states. Observations during the eROSITA survey detected a resurgence of activity in XMMSL2 J1404-2511 commensurate with flares repeating with a period of ~ 710 days and lending support to the idea that XMMSL2 J1404-2511 has experienced multiple partial tidal disruptions.

We find that a significantly higher fraction of TDEs with a hard X-ray component are found in an X-ray discovered sample than in an optically-selected sample, pointing towards a possible intrinsic difference in their properties. To exclude selection bias further monitoring of the optical sample is needed.

We recommend that any future TDE which shows an unusually rapid decay should continue to be monitored to check for repeat flares.

Acknowledgements

We thank the anonymous referee for constructive comments which improved the manuscript. We would like to thank the XMM OTAC for approving this program. The XMM-Newton project is an ESA science mission with instruments and contributions directly funded by ESA member states and the USA (NASA). The XMM-Newton project is supported by the Bundesministerium für Wirtschaft und Technologie/Deutsches Zentrum für Luft- und Raumfahrt (DLR) (FKZ 50 OX 0001), the Max-Planck Society and the Heidenhain-Stiftung. We thank the *Swift* team for approving and performing the monitoring observations. This work made use of data supplied by the UK *Swift* Science Data Centre at the University of Leicester. We thank the *NuSTAR* project scientist for allocating DDT time to this project. This research has made use of the NuSTAR Data Analysis Software (NuSTARDAS) jointly developed by the ASI Science Data Center (ASDC, Italy) and the California Institute of Technology (USA). This publication makes use of VOSA, developed under the Spanish Virtual Observatory (<https://svo.cab.inta-csic.es>) project funded by MCIN/AEI/10.13039/501100011033/ through grant PID2020-112949GB-I00. VOSA has been partially updated by using funding from the European Union's Horizon 2020 Research and Innovation Programme, under Grant Agreement n° 776403 (EXOPLANETS-A). Some of the data presented in this paper were obtained from the Mikulski Archive for Space Telescopes (MAST). STScI is operated by the Association of Universities for Research in Astronomy, Inc., under NASA contract NAS5-26555. RS would like to thank the late Tomaso Belloni for conversations along the years which helped to form some of the ideas in this paper. This work is based on data from eROSITA, the soft X-ray instrument aboard SRG, a joint Russian-German science mission supported by the Russian Space Agency (Roskosmos), in the interests of the Russian Academy of Sciences represented by its Space Research Institute (IKI), and the Deutsches Zentrum für Luft- und Raumfahrt (DLR). The SRG spacecraft was built by Lavochkin Association (NPOL) and its subcontractors, and is operated by NPOL with support from the Max Planck Institute for Extraterrestrial Physics (MPE). The development and construction of the eROSITA X-ray instrument was led by MPE, with contributions from the Dr. Karl Remeis Observatory Bamberg & ECAP (FAU Erlangen-Nürnberg), the University of Hamburg Observatory, the Leibniz Institute for Astrophysics Potsdam (AIP), and the Institute for Astronomy and Astrophysics of the University of Tübingen, with the support of DLR and the Max Planck Society. The Argelander Institute for Astronomy of the University of Bonn and the Ludwig Maximilians Universität Munich also participated in the science preparation for eROSITA. Some plots in this paper were produced using the *Veusz* software package (<http://veusz.github.io/>). GM acknowledges support from grants n. PID2020-115325GB-C31 and n. PID2023-147338NB-C21 funded by MICIU/AEI/10.13039/501100011033. MG is funded by Spanish MICIU/AEI/10.13039/501100011033 and ERDF/EU grant PID2023-147338NB-C21. KA acknowledges support provided by the National Science Foundation through award AST-2307668 and from the Alfred P. Sloan Foundation.

Data Availability

The data and scripts used in this paper will be made available on Zenodo post-publication. The Zenodo doi is 10.5281/zenodo.14601857.

References

- Abramowicz, M. A., Czerny, B., Lasota, J. P., & Szuszkiewicz, E. 1988, *ApJ*, 332, 646
- Ajay, Y., Pasham, D., & Guolo, M. 2022, *The Astronomer's Telegram*, 15724, 1
- Akylas, A. & Georgantopoulos, I. 2021, *A&A*, 655, A60
- Alexander, K. D., van Velzen, S., Horesh, A., & Zauderer, B. A. 2020, *Space Sci. Rev.*, 216, 81
- Arcavi, I., Gal-Yam, A., Sullivan, M., et al. 2014, *ApJ*, 793, 38
- Arcodia, R., Merloni, A., Nandra, K., et al. 2021, *Nature*, 592, 704
- Arnaud, K. A. 1996, in *Astronomical Society of the Pacific Conference Series*, Vol. 101, *Astronomical Data Analysis Software and Systems V*, ed. G. H. Jacoby & J. Barnes, 17
- Auchettl, K., Guillochon, J., & Ramirez-Ruiz, E. 2017, *ApJ*, 838, 149
- Ballantyne, D. R., Sudhakar, V., Fairfax, D., et al. 2024, *MNRAS*, 530, 1603
- Belloni, T., Méndez, M., King, A. R., van der Klis, M., & van Paradijs, J. 1997, *ApJ*, 479, L145
- Bianchi, L., Shiao, B., & Thilker, D. 2017, *ApJS*, 230, 24
- Bloom, J. S., Giannios, D., Metzger, B. D., et al. 2011, *Science*, 333, 203
- Bright, J. S., Fender, R. P., Motta, S. E., et al. 2018, *MNRAS*, 475, 4011
- Brown, J. S., Holoien, T. W. S., Auchettl, K., et al. 2017, *MNRAS*, 466, 4904
- Brunner, H., Liu, T., Lamer, G., et al. 2022, *A&A*, 661, A1
- Burrows, D. N., Kennea, J. A., Ghisellini, G., et al. 2011, *Nature*, 476, 421
- Cannizzo, J. K., Lee, H. M., & Goodman, J. 1990, *ApJ*, 351, 38
- Cao, Z., Jonker, P. G., Pasham, D. R., et al. 2024, *ApJ*, 970, 89
- Cao, Z., Jonker, P. G., Wen, S., Stone, N. C., & Zabludoff, A. I. 2023, *MNRAS*, 519, 2375
- Cappellari, M. 2017, *MNRAS*, 466, 798
- Chakraborty, J., Kara, E., Masterson, M., et al. 2021, *ApJ*, 921, L40
- Christy, C. T., Alexander, K. D., Cendes, Y., et al. 2024, *arXiv e-prints*, arXiv:2404.12431
- Conroy, C., Gunn, J. E., & White, M. 2009, *ApJ*, 699, 486
- Coughlin, E. R. & Nixon, C. J. 2019, *ApJ*, 883, L17
- Dai, L., McKinney, J. C., Roth, N., Ramirez-Ruiz, E., & Miller, M. C. 2018, *ApJ*, 859, L20
- Dey, A., Schlegel, D. J., Lang, D., et al. 2019, *AJ*, 157, 168
- Done, C., Davis, S. W., Jin, C., Blaes, O., & Ward, M. 2012, *MNRAS*, 420, 1848
- Done, C., Mulchaey, J. S., Mushotzky, R. F., & Arnaud, K. A. 1992, *ApJ*, 395, 275
- Dubus, G., Hameury, J. M., & Lasota, J. P. 2001, *A&A*, 373, 251
- Esin, A. A., McClintock, J. E., & Narayan, R. 1997, *ApJ*, 489, 865
- Esquej, P., Saxton, R. D., Komossa, S., et al. 2008, *A&A*, 489, 543
- Evans, P. A., Beardmore, A. P., Page, K. L., et al. 2009, *MNRAS*, 397, 1177
- Gabriel, C., Denby, M., Fyfe, D. J., et al. 2004, in *Astronomical Society of the Pacific Conference Series*, Vol. 314, *Astronomical Data Analysis Software and Systems (ADASS) XIII*, ed. F. Ochsenbein, M. G. Allen, & D. Egret, 759
- Gallo, L. C., Boller, T., Tanaka, Y., et al. 2004, *MNRAS*, 347, 269
- Gehrels, N., Chincarini, G., Giommi, P., et al. 2004, *ApJ*, 611, 1005
- Gezari, S. 2021, *ARA&A*, 59, 21
- Gezari, S., Cenko, S. B., & Arcavi, I. 2017, *ApJ*, 851, L47
- Gezari, S., Halpern, J. P., Komossa, S., Grupe, D., & Leighly, K. M. 2003, *ApJ*, 592, 42
- Giustini, M., Miniutti, G., & Saxton, R. D. 2020, *A&A*, 636, L2
- Greene, J. E., Strader, J., & Ho, L. C. 2020, *ARA&A*, 58, 257
- Gronkiewicz, D. & Różańska, A. 2020, *A&A*, 633, A35
- Gronkiewicz, D., Różańska, A., Petrucci, P.-O., & Belmont, R. 2023, *A&A*, 675, A198
- Grünwald, G., Boller, T., Rakshit, S., et al. 2023, *A&A*, 669, A37
- Gruzinov, A. V. 1998, *ApJ*, 501, 787
- Guillochon, J. & Ramirez-Ruiz, E. 2013, *ApJ*, 767, 25
- Gültekin, K., Richstone, D. O., Gebhardt, K., et al. 2009, *ApJ*, 698, 198
- Guolo, M., Gezari, S., Yao, Y., et al. 2024, *ApJ*, 966, 160
- Guolo, M. & Mummery, A. 2025, *ApJ*, 978, 167
- Hajela, A., Alexander, K. D., Margutti, R., et al. 2025, *ApJ*, 983, 29
- Hammerstein, E., van Velzen, S., Gezari, S., et al. 2023, *ApJ*, 942, 9
- Harrison, F. A., Craig, W. W., Christensen, F. E., et al. 2013, *ApJ*, 770, 103
- Hart, K., Shappee, B. J., Hey, D., et al. 2023, *arXiv e-prints*, arXiv:2304.03791
- Hills, J. G. 1975, *Nature*, 254, 295
- Hodgkin, S. T., Harrison, D. L., Breed, E., et al. 2021, *A&A*, 652, A76
- Holoien, T. W. S., Kochanek, C. S., Prieto, J. L., et al. 2016, *MNRAS*, 455, 2918
- Holoien, T. W. S., Prieto, J. L., Bersier, D., et al. 2014, *MNRAS*, 445, 3263
- Janiuk, A., Czerny, B., & Madejski, G. M. 2001, *ApJ*, 557, 408
- Jansen, F., Lumb, D., Altieri, B., et al. 2001, *A&A*, 365, L1
- Jiang, N., Dou, L., Wang, T., et al. 2016, *ApJ*, 828, L14
- Jin, C. C., Li, D. Y., Jiang, N., et al. 2025, *arXiv e-prints*, arXiv:2501.09580
- Johnson, B. & Leja, J. 2017, *bd-j/prospector: Initial release*
- Jonker, P. G., Stone, N. C., Generozov, A., van Velzen, S., & Metzger, B. 2020, *ApJ*, 889, 166
- Kajava, J. J. E., Sánchez-Fernández, C., Alfonso-Garzón, J., Motta, S. E., & Veleidina, A. 2020, *A&A*, 634, A94
- Kalemci, E., Dinçer, T., Tomsick, J. A., et al. 2013, *ApJ*, 779, 95
- Komossa, S. 2004, in *IAU Symposium*, Vol. 222, *The Interplay Among Black Holes, Stars and ISM in Galactic Nuclei*, ed. T. Storchi-Bergmann, L. C. Ho, & H. R. Schmitt, 45–48
- Komossa, S. 2015, *Journal of High Energy Astrophysics*, 7, 148
- Komossa, S. & Bade, N. 1999, *A&A*, 343, 775
- Kubota, A. & Done, C. 2018, *MNRAS*, 480, 1247
- Laha, S., Ricci, C., Mather, J. C., et al. 2024, *arXiv e-prints*, arXiv:2412.11321
- Li, D., Saxton, R. D., Yuan, W., et al. 2020, *ApJ*, 891, 121
- Li, R., Ricci, C., Ho, L. C., et al. 2024, *ApJ*, 975, 140
- Lin, D., Guillochon, J., Komossa, S., et al. 2017, *Nature Astronomy*, 1, 0033
- Linial, I. & Metzger, B. D. 2024, *ApJ*, 973, 101
- Liu, Z., Malyali, A., Krumpke, M., et al. 2023, *A&A*, 669, A75
- Liu, Z., Ryu, T., Goodwin, A. J., et al. 2024, *A&A*, 683, L13
- Maccarone, T. J. 2003, *A&A*, 409, 697
- Magdziarz, P., Blaes, O. M., Zdziarski, A. A., Johnson, W. N., & Smith, D. A. 1998, *MNRAS*, 301, 179
- Magdziarz, P. & Zdziarski, A. A. 1995, *MNRAS*, 273, 837
- Mainzer, A., Bauer, J., Grav, T., et al. 2011, *ApJ*, 731, 53
- Maitra, D. & Bailyn, C. D. 2006, *ApJ*, 637, 992
- Malyali, A., Liu, Z., Rau, A., et al. 2023, *MNRAS*, 520, 3549
- Marconi, A. & Hunt, L. K. 2003, *ApJ*, 589, L21
- Martin, D. C., Fanson, J., Schiminovich, D., et al. 2005, *ApJ*, 619, L1
- Miniutti, G., Saxton, R. D., Giustini, M., et al. 2019, *Nature*, 573, 381
- Miniutti, G., Saxton, R. D., Rodríguez-Pascual, P. M., et al. 2013, *MNRAS*, 433, 1764
- Mou, G., Dou, L., Jiang, N., et al. 2021, *ApJ*, 908, 197
- Mummery, A. 2021, *MNRAS*, 507, L24
- Mummery, A. & Balbus, S. A. 2020, *MNRAS*, 492, 5655
- Mummery, A. & van Velzen, S. 2024, *arXiv e-prints*, arXiv:2410.17087
- Mummery, A., van Velzen, S., Nathan, E., et al. 2024, *MNRAS*, 527, 2452
- Mummery, A., Wevers, T., Saxton, R., & Pasham, D. 2023, *MNRAS*, 519, 5828
- Nishimura, J., Mitsuda, K., & Itoh, M. 1986, *PASJ*, 38, 819
- Nixon, C. J., Coughlin, E. R., & Miles, P. R. 2021, *ApJ*, 922, 168
- Ohsuga, K., Mineshige, S., Mori, M., & Umemura, M. 2002, *ApJ*, 574, 315
- Ojha, V., Chand, H., Dewangan, G. C., & Rakshit, S. 2020, *ApJ*, 896, 95
- Palit, B., Różańska, A., Petrucci, P. O., et al. 2024, *A&A*, 690, A308
- Petrucci, P. O., Ursini, F., De Rosa, A., et al. 2018, *A&A*, 611, A59
- Piran, T., Svirski, G., Krolik, J., Cheng, R. M., & Shiokawa, H. 2015, *ApJ*, 806, 164
- Piro, A. L. & Mockler, B. 2025, *ApJ*, 985, 77
- Plotkin, R. M., Gallo, E., & Jonker, P. G. 2013, *ApJ*, 773, 59
- Ponti, G., Papadakis, I., Bianchi, S., et al. 2012, *A&A*, 542, A83
- Predehl, P., Andritschke, R., Arefiev, V., et al. 2021, *A&A*, 647, A1
- Prugniel, P., Soubiran, C., Koleva, M., & Le Borgne, D. 2007, *arXiv e-prints*, astro
- Rao, A. R., Yadav, J. S., & Paul, B. 2000, *ApJ*, 544, 443
- Read, A. M., Saxton, R., Komossa, S., Alexander, K. D., & Maksym, W. P. 2018, *The Astronomer's Telegram*, 11394, 1
- Rees, M. J. 1988, *Nature*, 333, 523
- Rees, M. J. 1990, *Science*, 247, 817
- Reeves, J., Done, C., Pounds, K., et al. 2008, *Monthly Notices of the Royal Astronomical Society: Letters*, 385, L108–L112
- Remillard, R. A. & McClintock, J. E. 2006, *ARA&A*, 44, 49
- Ricci, C., Kara, E., Loewenstein, M., et al. 2020, *ApJ*, 898, L1
- Ricci, C. & Trakhtenbrot, B. 2022, *arXiv e-prints*, arXiv:2211.05132
- Ruan, J. J., Anderson, S. F., Eracleous, M., et al. 2019, *ApJ*, 883, 76
- Ryu, T., Krolik, J., Piran, T., & Noble, S. C. 2020, *ApJ*, 904, 100
- Saxton, R., Komossa, S., Auchettl, K., & Jonker, P. G. 2021, *Correction to: X-Ray Properties of TDEs*, *Space Science Reviews*, Volume 217, Issue 1, article id.18
- Saxton, R. D., Motta, S. E., Komossa, S., & Read, A. M. 2015, *MNRAS*, 454, 2798
- Saxton, R. D., Read, A. M., Esquej, P., et al. 2012, *A&A*, 541, A106
- Saxton, R. D., Read, A. M., Komossa, S., et al. 2019, *A&A*, 630, A98
- Saxton, R. D., Read, A. M., Komossa, S., et al. 2017, *A&A*, 598, A29
- Saxton, R. D., Read, A. M., Komossa, S., et al. 2014, *A&A*, 572, A1
- Sazonov, S., Gilfanov, M., Medvedev, P., et al. 2021, *MNRAS*, 508, 3820
- Shappee, B., Prieto, J., Stanek, K. Z., et al. 2014, in *American Astronomical Society Meeting Abstracts*, Vol. 223, *American Astronomical Society Meeting Abstracts #223*, 236.03
- Shen, R.-F. & Matzner, C. D. 2014, *ApJ*, 784, 87
- Smartt, S., Valenti, S., Fraser, M., et al. 2015, *A&A*, 579
- Steinberg, E. & Stone, N. C. 2022, *arXiv e-prints*, arXiv:2206.10641
- Steiner, J. F., Narayan, R., McClintock, J. E., & Ebisawa, K. 2009, *PASP*, 121, 1279
- Stern, D., Assef, R. J., Benford, D. J., et al. 2012, *ApJ*, 753, 30
- Svoboda, J., Guainazzi, M., & Merloni, A. 2017, *A&A*, 603, A127
- Tamborra, F., Papadakis, I., Dovčiak, M., & Svoboda, J. 2018, *MNRAS*, 475, 2045

- Taubenberger, S., Floers, A., Vogl, C., et al. 2018, *The Astronomer's Telegram*, 11395, 1
- Titarchuk, L. 1994, *ApJ*, 434, 570
- Ulmer, A. 1999, *ApJ*, 514, 180
- van Velzen, S., Gezari, S., Hammerstein, E., et al. 2021, *ApJ*, 908, 4
- Wang, Y., Pasham, D. R., Altamirano, D., et al. 2024, *ApJ*, 962, 78
- Wen, S., Jonker, P. G., Stone, N. C., Van Velzen, S., & Zabludoff, A. I. 2023, *MNRAS*, 522, 1155
- Wen, S., Jonker, P. G., Stone, N. C., Zabludoff, A. I., & Psaltis, D. 2020, *ApJ*, 897, 80
- Wevers, T. 2020, *MNRAS*, 497, L1
- Wevers, T., Coughlin, E. R., Pasham, D. R., et al. 2023, *ApJ*, 942, L33
- Wevers, T., Guolo, M., Pasham, D. R., et al. 2024, *ApJ*, 963, 75
- Wevers, T., Pasham, D. R., Jalan, P., Rakshit, S., & Arcodia, R. 2022, *A&A*, 659, L2
- Wevers, T., Pasham, D. R., van Velzen, S., et al. 2019, *Monthly Notices of the Royal Astronomical Society*, 488, 4816
- Wevers, T., Pasham, D. R., van Velzen, S., et al. 2021, *ApJ*, 912, 151
- Wevers, T., van Velzen, S., Jonker, P. G., et al. 2017, *MNRAS*, 471, 1694
- Willingale, R., Starling, R. L. C., Beardmore, A. P., Tanvir, N. R., & O'Brien, P. T. 2013, *MNRAS*, 431, 394
- Wilms, J., Allen, A., & McCray, R. 2000, *ApJ*, 542, 914
- Wright, E. L., Eisenhardt, P. R. M., Mainzer, A. K., et al. 2010, *AJ*, 140, 1868
- Yao, Y. & Guolo, M. 2022, *The Astronomer's Telegram*, 15657, 1
- Yao, Y., Lu, W., Guolo, M., et al. 2022, *ApJ*, 937, 8
- Yuan, W., Komossa, S., Zhang, C., et al. 2016, in *IAU Symposium*, Vol. 312, *Star Clusters and Black Holes in Galaxies across Cosmic Time*, ed. Y. Meiron, S. Li, F. K. Liu, & R. Spurzem, 68–70
- Zauderer, B. A., Berger, E., Margutti, R., et al. 2013, *ApJ*, 767, 152
- Zdziarski, A. A., Szanecki, M., Poutanen, J., Gierliński, M., & Biernacki, P. 2020, *MNRAS*, 492, 5234

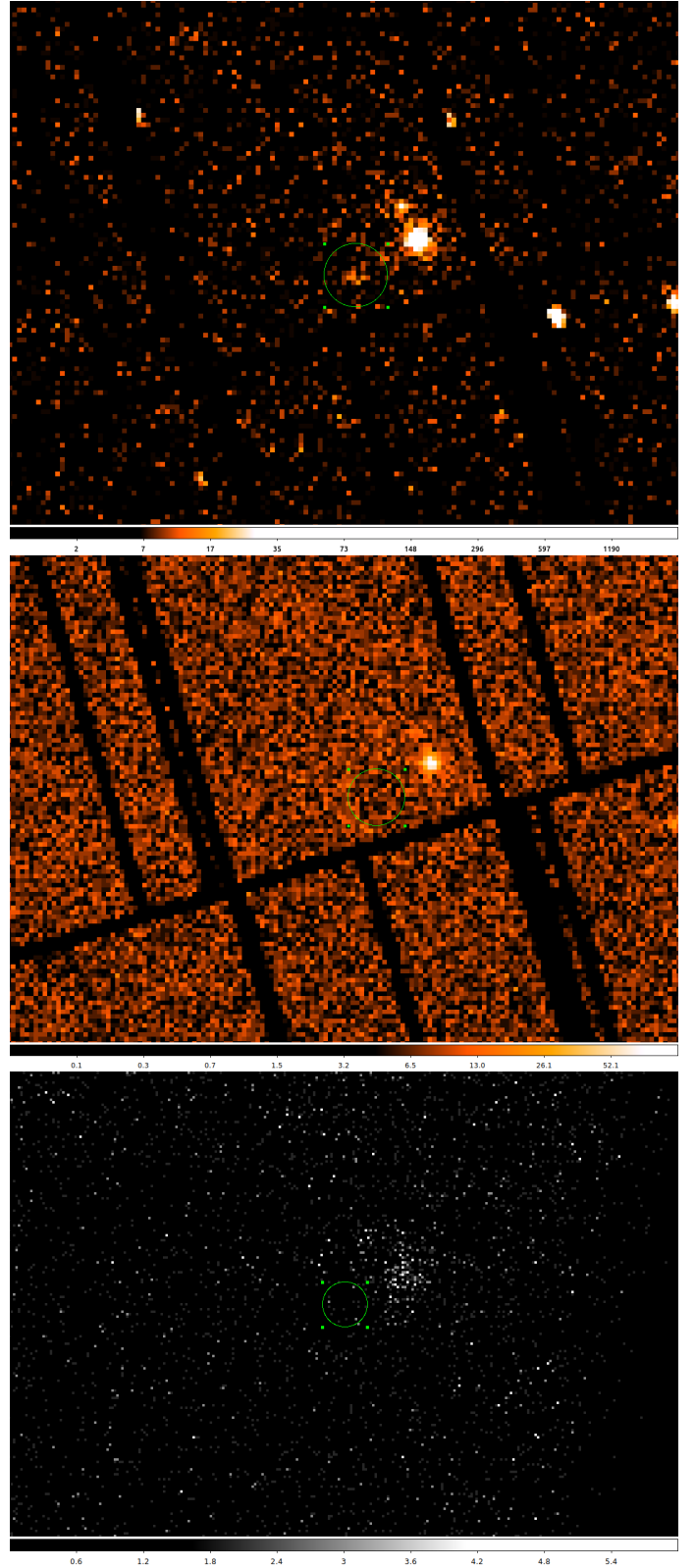


Fig. 10. Upper: EPIC-pn, 0.2-2 keV image of XMMSL2 J1404-2511 taken on 2019-01-10, Middle: EPIC-pn, 2-10 keV image, Lower: NuSTAR, FPA, 3-100 keV image centred on the position of XMMSL2 J1404-2511. The source, whose position is denoted by a green circle, is not detected in the latter two images.

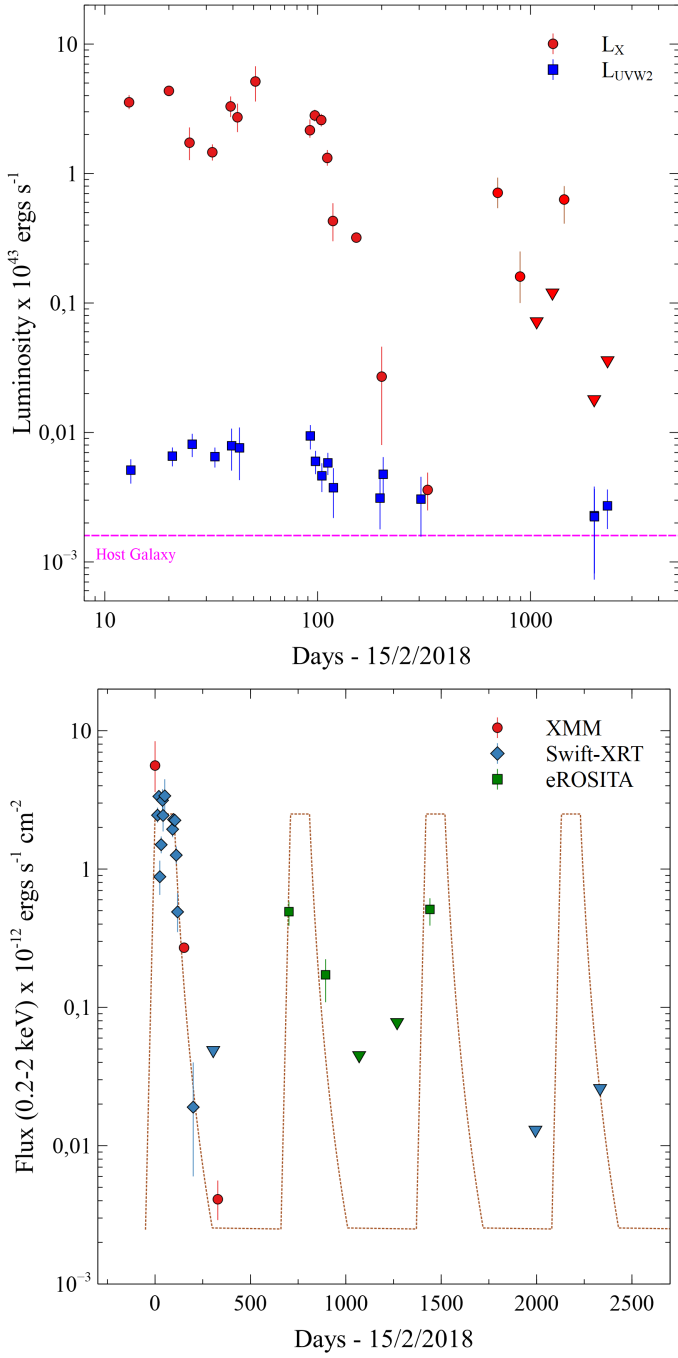


Fig. 11. Upper: X-ray (red circles) and host-subtracted, Galactic absorption-corrected, UVOT-UVW2 filter (blue squares) luminosity light curves. The modelled host galaxy UVW2 luminosity is shown for reference (pink dashed line). Lower: Full X-ray observed flux light curve calculated using the *COMPBB* model (see Tab. 3). The dotted line represents a flare consisting of a 50 day rise to a 100 day plateau of 2.5×10^{-12} ergs $s^{-1}cm^{-2}$ and a 200 day decay with index t^{-5} , repeating every 710 days. Downward triangles denote 2-sigma upper limits.

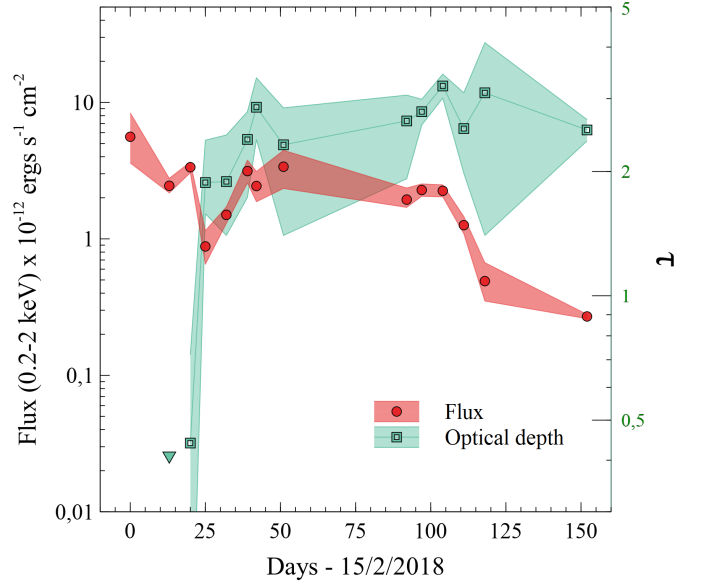


Fig. 12. Optical depth and observed 0.2–2 keV flux for the first 152 days of observations of XMMSL2 J1404-2511 using a spectral model of *COMPBB* with $kT_e = 5$ keV. The shaded areas represent 90% confidence intervals on the measured parameters.

Appendix A: Spectral analysis of the adjacent source 2SXPS J140442.5-251104

Spectral products were extracted from *Swift* -XRT observations of the source, 2SXPS J140442.5-251104, which lies at a distance of 67 arcseconds from XMMSL2 J1404-2511, using the on-line XRT data products tool. A fit was performed yielding a good fit ($\chi^2_r = 54/56$) for a power-law of slope $\Gamma = 1.66^{+0.13}_{-0.12}$, absorbed by the Galactic column of $N_H = 6.7 \times 10^{20} \text{ cm}^{-2}$ and a further intrinsic absorber of $N_{H,i} = 2.3 \pm 0.5 \times 10^{21} \text{ cm}^{-2}$ both modelled with the *TBABS* model. No appreciable variability was found in the light curve of the source with in-band fluxes of $F_{0.2-2 \text{ keV}} = 5.5 \times 10^{-14} \text{ ergs s}^{-1} \text{ cm}^{-2}$ and $F_{2-10 \text{ keV}} = 1.9 \times 10^{-13} \text{ ergs s}^{-1} \text{ cm}^{-2}$.

Appendix B: X-ray short-term light curve and black hole mass

In Fig. B.1 we show the 0.2-2 keV light curve of the 2018-07-17 XMM-*Newton* observation. This has a minimum doubling time of about 200s. Applying the relationship between X-ray variability and mass derived in Ponti et al. (2012) we obtain a black hole mass of $2.5^{+4.2}_{-1.6} \times 10^6 M_\odot$. From the K magnitude and the correlation of Marconi & Hunt (2003) we find a mass of $4.5^{+4.4}_{-2.3} \times 10^6 M_\odot$. The mass obtained from fitting the optical spectrum line widths was $M_{BH} = 5.1^{+9.0}_{-3.2} \times 10^6 M_\odot$ (Section 3). We can also use the X-ray spectral properties to estimate M_{BH} . We fit the thermally-dominated, first *Swift* -XRT observation (S1) with an accretion disc model (*TDEDISCSPEC*; Mummery et al. 2023), obtaining a radius $R_p = 6.1^{+3.3}_{-1.5} \times 10^{11} \text{ cm}$ and peak temperature $T_p = 6.5^{1.0}_{0.6} \times 10^5 \text{ K}$ (56^{+9}_{-5} eV). From the relationship between R_p and M_{BH} given in Mummery et al. (2023) we derive $M_{BH} = 3.0^{+4.3}_{-1.8} \times 10^6 M_\odot$. Finally, using the galaxy stellar mass of $\log M_* = 10.4$, obtained from the SED fit shown in Fig. 3, and the relationship given in (Greene et al. 2020), we derive $M_{BH} = 2 \times 10^7 M_\odot$ with a systematic error of 0.8 dex.

As all mass measurements are consistent within the errors we adopt $M_{BH} = 4^{+2}_{-2} \times 10^6 M_\odot$.

We barycentre-corrected the light curve, binned it into 10 second bins and exposure corrected with the *epiclccorr* task, from the SAS software (Gabriel et al. 2004), to search for any periodicity. None was found.

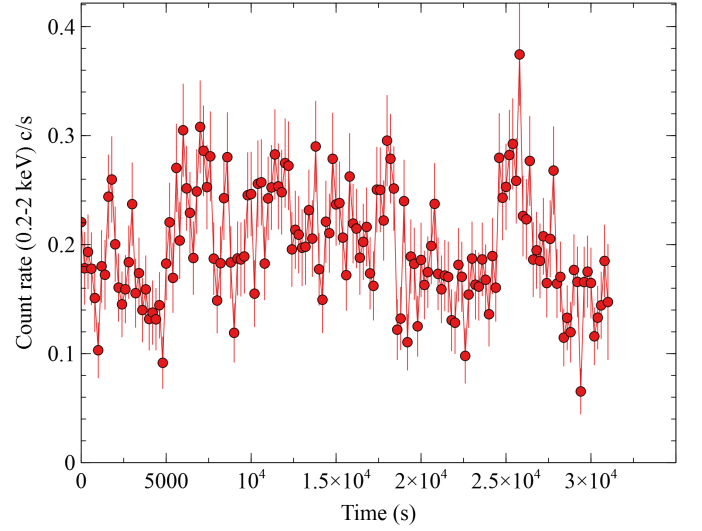


Fig. B.1. Soft X-ray light curve of XMMSL2 J1404-2511 from the XMM-*Newton* pointed observation of 2018-07-17, binned into 200s bins.